

# Combined Fit of Spectrum and Composition for FR0 Radio Galaxy Emitted Ultra-High-Energy Cosmic Rays with Resulting Secondary Photons and Neutrinos

Jon Paul Lundquist<sup>a,\*</sup>, Serguei Vorobiov<sup>a</sup>, Lukas Merten<sup>b,c</sup>, Anita Reimer<sup>d</sup>, Margot Boughelilba<sup>d</sup>, Paolo Da Vela<sup>d</sup>, Fabrizio Tavecchio<sup>e</sup>, Giacomo Bonnoli<sup>f</sup>, Chiara Righi<sup>e</sup>

<sup>a</sup>Center for Astrophysics and Cosmology (CAC), University of Nova Gorica, Vipavska 13, SI-5000 Nova Gorica, Slovenia

<sup>b</sup>Institute for Theoretical Physics IV, Faculty for Physics and Astronomy, Ruhr University Bochum, Universitätsstraße 150, 44801 Bochum, Germany

<sup>c</sup>Ruhr Astroparticle and Plasma Physics Center (RAPP Center), Bochum, Germany

<sup>d</sup>Institute for Astro and Particle Physics, University of Innsbruck, Technikerstraße 25, 6020 Innsbruck, Austria

<sup>e</sup>Astronomical Observatory of Brera, Via Brera 28, 20121 Milano, Italy

<sup>f</sup>Instituto de Astrofísica de Andalucía (CSIC), Apartado 3004, E-18080 Granada, Spain

---

## Abstract

This study comprehensively investigates the gamma-ray dim population of Fanaroff-Riley Type 0 (FR0) radio galaxies as potentially significant sources of ultra-high-energy cosmic rays (UHECRs,  $E > 10^{18}$  eV) detected on Earth. While individual FR0 luminosities are relatively low compared to the more powerful Fanaroff-Riley Type 1 and Type 2 galaxies, FR0s are substantially more prevalent in the local universe, outnumbering the more energetic galaxies by a factor of  $\sim 5$  within a redshift of  $z \leq 0.05$ .

Employing CRPropa3 simulations, we estimate the mass composition and energy spectra of UHECRs originating from FR0 galaxies for energies above  $10^{18.6}$  eV. This estimation fits data from the Pierre Auger Observatory (Auger) using three extensive air shower models; both constant and energy-dependent observed elemental fractions are considered. The simulation integrates an isotropic distribution of FR0 galaxies, extrapolated from observed characteristics, with UHECR propagation in the intergalactic medium, incorporating various plausible configurations of extragalactic magnetic fields, both random and structured. We then compare the resulting emission spectral indices, rigidity cutoffs, and elemental fractions with recent Auger results. In total, 25 combined energy spectrum and mass composition fits are considered.

Beyond the cosmic ray fluxes emitted by FR0 galaxies, this study predicts the secondary photon and neutrino fluxes from UHECR interactions with intergalactic cosmic photon backgrounds. The multi-messenger approach, encompassing observational data and theoretical models, helps elucidate the contribution of low luminosity FR0 radio galaxies to the total cosmic ray energy density.

*Keywords:* Ultra-high-energy-cosmic radiation (1733), Fanaroff-Riley radio galaxies (526), Low-luminosity AGN (2033), Extragalactic magnetic fields (507), Cosmic background radiation (317), Gamma-rays (637), Neutrino astronomy (1100), Cosmic ray showers (327)

## 1. Introduction

Ultra-high-energy cosmic rays (UHECRs) are the most energetic particles observed in the Universe, with energies exceeding  $10^{18}$  eV. Their origins are an open astrophysical question, with potential sources including active galactic nuclei (AGN), various radio galaxies, gamma-ray bursts, and starburst galaxies. The Pierre Auger Observatory (Auger), located in Argentina, was established as the largest ( $\sim 3000$  km<sup>2</sup>) UHECR hybrid detector in the world to study these particles [1]. Auger provides the highest statistics data on the energy spectra, composition, and arrival directions of UHECR, offering essential information to explore their sources and propagation mechanisms.

Low luminosity Fanaroff-Riley (FR0 Class) radio galaxies [2] (radio-loud jetted AGN) have emerged as a promising candidate class of sources of UHECRs detected on Earth. Recent surveys have highlighted that FR0s are approximately five times more prevalent in the local universe compared to their more energetic counterparts, Fanaroff-Riley Type 1 (FR1) and Type 2 sources [3], qualifying them as potentially substantial contributors to the UHECR energy density. Despite their similar core radio properties to FR1s [4], FR0s display much weaker extended radio emission; however, their estimated jet power, which significantly exceeds the required cosmic ray power per source [5], suggests they could substantially contribute to the UHECR flux measured on Earth. Studies utilizing the average FR0 spectral energy distribution suggest that these galaxies can accelerate UHECRs to the high-

---

\*Corresponding author

Email address: [jlundquist@ung.si](mailto:jlundquist@ung.si) (Jon Paul Lundquist)

est observed energies through hybrid acceleration, combining Fermi-I pre-acceleration with gradual shear acceleration [6]. Therefore, they fulfill both the Hillas criterion [7] and the energetics criteria [8, 9].

Multi-messenger astrophysics, which involves the combined study of various cosmic messengers such as photons, neutrinos, and cosmic rays, offers an even more comprehensive understanding of astrophysical phenomena. This approach helps identify and characterize sources of UHECRs and refine our knowledge of the mechanisms that generate and propagate these particles. Regarding the multi-messenger properties of FR0s, leptohadronic jet-disc modeling of core-emission from quiet low luminosity AGN jets predicts that FR0s are expected to be relatively weak gamma-ray and neutrino emitters [10, 11]. This theoretical evaluation of weak multi-messenger emission aligns with the results of searches for gamma-ray emitting FR0 galaxies. For example, stacking analyses were necessary to detect a very small unresolved FR0 population in *Fermi*-LAT data and identify them as gamma-ray emitters [12, 13]. A recent study [14] using various *Fermi*-LAT catalogs as sources of cosmic rays in CRPropa simulations concluded that previously resolved (therefore overwhelmingly non-FR0) gamma-ray sources cannot account for the large-scale anisotropy of UHECR events above 8 EeV as established by the Pierre Auger Collaboration [15]. This discrepancy led the authors of [14] to conclude that another population of UHECR sources, either lacking gamma-ray emission or unresolved by current-generation telescopes, must exist.

The effect on expected arrival distribution of diffuse UHECRs in the intergalactic magnetic field has been examined in several studies, e.g., in [16, 17, 18] that provide constraints on the source emission spectra and composition (e.g., [19, 20]). The Auger large angular scale arrival direction analysis points to the extragalactic origins of UHECR for energies  $E \geq 8$  EeV [15]. A recent three-component combined fit of the UHECR energy spectrum, extensive air shower (EAS) maxima distributions ( $X_{\max}$ ), and arrival directions supports an astrophysical model primarily comprised of homogeneous background sources and an adaptable addition from nearby source candidates [21]. For instance, if these additional nearby sources are a selection of 44 starburst galaxies, they could contribute up to a  $\sim 20\%$  flux fraction at 40 EeV [21] — a sizable fraction of the remaining bulk of UHECRs may be from FR0s.

However, a considerable uncertainty in the strength and configuration of intergalactic magnetic fields confounds the extrapolation of UHECR measurements to their potential sources. Assuming a primordial field, theoretical modeling of the Universe’s evolution results in structured field models with an average magnitude on the order of  $\sim 10^{-11}$  gauss [22, 23]. In contrast, fitting UHECR propagation simulations to data is a good fit with an average field magnitude of  $\sim 1$  nG [24, 25].

In this study, we leverage the strengths of multi-messenger observations to investigate the properties of FR0 ra-

dio galaxies as potential UHECR sources. We simulate isotropic FR0 UHECR emission, extrapolating from measured FR0 properties and propagating them to Earth through plausible intergalactic magnetic fields using CRPropa3 [26]. By a combined fit of these simulations to energy and composition using Pierre Auger Observatory data [27, 28], we estimate the UHECR mass composition and energy spectra emitted by FR0s. These combined energy spectrum and composition fits are done using two nuclei emission composition models - a constant nuclei composition emission over the energy range and an evolving emission that depends on energy. Additionally, we present estimates of the cosmogenic secondary photon and neutrino fluxes resulting from UHECR interactions with cosmic photon backgrounds.

## 2. Pierre Auger Observatory Data

Auger performs high-precision and large-statistics analyses of energy spectra, mass composition, and arrival directions of UHECR data which are essential for assessing theoretical models of cosmic ray origins and propagation. This study utilizes the energy spectrum and composition datasets to systematically extrapolate the observed characteristics of UHECRs to predictions of FR0 galaxy emission. The Auger data used in fitting simulations of FR0 radio galaxy UHECR emission is the publicly available energy spectrum from [28] and composition from [27] (using the method of [29]) for energies  $E \geq 10^{18.6}$  eV. These results using 13 years of data are shown in Figure 6. The composition is given in terms of mean log mass number  $\langle \ln A \rangle$ , which is evaluated from fluorescence detector determined depth of shower maximum  $X_{\max}$  using three different extensive air-shower (EAS) models – Sibyll2.3c [30], EPOS-LHC [31], and QGSJetII-04 [32]. These are referred to in the following figures, tables, and in combination with magnetic field models as SIBYLL, EPOS, and QGS4 for brevity.

## 3. Propagation Framework

The open-source CRPropa3 (v3.2) framework [26] is used to simulate UHECR primary nuclei propagation through intergalactic media. This software models interactions with cosmic backgrounds and deflections in magnetic fields, allowing us to trace the trajectories, composition, and energy changes of UHECRs from their sources to Earth. The five primary nuclei of hydrogen, helium, nitrogen, silicon, and iron are generated with an emission energy spectrum  $dN/dE \propto E_0^{-1}$ , with energies  $E_0$  ranging from  $10^{18.6}$  eV to  $10^{21}$  eV. This  $\gamma = 1$  spectrum is generated for more statistics at the highest energies, and simulated events are reweighted for the combined fit to the data.

Simulated UHECR interactions with the intergalactic cosmic microwave, UV, optical, IR (Gilmore12 model

[33]), and radio (Protheroe96 model [34]) photon backgrounds account for photopion production, nuclear photo-disintegration, Bethe-Heitler process, gamma-gamma pair-production (single, double, and triplet), and inverse Compton scattering. Additionally, universe expansion adiabatic energy loss and unstable nuclear decays are considered.

The CRPropa3 observer used is a 200 kpc sphere centered at the Milky Way center and intersecting nuclei are recorded for energies  $E \geq 10^{18.6}$  eV. Additional interactions and deflections in the last 200 kpc are expected to be negligible. Particles intersecting with another sphere  $\sim 2$  Gpc in radius or traveling further than 4 Gpc were discarded. Secondary neutrinos with energies above 100 TeV that intersect the observer are recorded. Secondary photons with energies above 100 MeV are immediately recorded if a projected linear path intersects the observer and are then propagated using the `DintElecaPropagation` module [35, 36].

### 3.1. Magnetic Fields

Charged nuclei deflections were simulated using four magnetic field models and a no magnetic field scenario. Two fields are turbulent and homogeneous with a mean strength  $\langle B \rangle = 1$  nG ( $B_{\text{RMS}} = 1.1$  nG) and length scales from 60 kpc to 1 Mpc (or 3 Mpc) and a Kolmogorov power spectrum for an average correlation length of  $l_{\text{corr}} = 234$  kpc referred to as Rand.A (or  $l_{\text{corr}} = 647$  kpc, Rand.B). The third model uses the Dolag et al. structured field [22], while the fourth employs the Hackstein et al. (CLUES) 'astrophysical1R' structured field [23]. Figure 1 shows the magnetic field strength distributions. This sampled range of magnetic fields are within theoretical expectations and were chosen based on their prevalence in recent UHECR studies and their expected impact on the propagation outcomes.

The Dolag et al. field [22] was created via a magnetohydrodynamic simulation of the primordial evolution of the local universe in a cube 340 Mpc on a side (repeated in simulation as needed) and has structures that are well corresponded with nearby galaxy clusters (Coma, Virgo, Centaurus, Hydra, Perseus, and A3627). The field also includes large-scale structures such as sheets and filaments. Though the average magnetic field is small ( $\langle B \rangle = 0.047$  nG), the largest fields are on the order of  $\sim 10$   $\mu\text{G}$ . Though these high magnitude fields are a small proportion of the volume, this results in the large  $B_{\text{RMS}} = 11$  nG. The reported expectation is that ultra-high-energy protons will, on average, have a smaller deflection than experimental sensitivities [22].

The Hackstein et al. (CLUES) structured fields [23] were also created via magnetohydrodynamic simulations within a smaller cube of 250 Mpc. The 'astrophysical1R' field (a nearly identical distribution to 'astrophysicalR') was chosen from the six CLUES fields. This field includes gas cooling and AGN feedback effects and also has structures corresponding with some nearby galaxy clusters (Coma, Centaurus, and Perseus) connected by strong

filaments. Though the average magnetic field is larger than the one from Dolag et al. ( $\langle B \rangle = 0.064$  nG) due to a more substantial background, the largest fields are on the order of 100 times less ( $\sim 0.1$   $\mu\text{G}$ ), resulting in a smaller  $B_{\text{RMS}} = 1.2$  nG. It is reported that a dipole amplitude is observed with a pure iron emission from isotropic sources [23].

## 4. Simulating FR0s as UHECR Sources

The simulated set of FR0s is upsampled from the well-sampled sky portion of the FROCAT catalog [3] (limited to  $z \leq 0.05$ ) and extrapolated to a redshift  $z \leq 0.2$  distance. This area is the spherical rectangle in supergalactic coordinates of  $-45^\circ$  to  $45^\circ$  SGB (latitude) and  $60^\circ$  to  $120^\circ$  SGL (longitude) (for a solid angle  $\Omega = \pi/3\sqrt{2}$ ), as shown in Figure 2 on the left. Inside this 11.79% sky coverage there are 76 cataloged FR0s within  $z \leq 0.05$  that appear isotropically distributed. Upsampling these data results in 645 FR0s, also with isotropically distributed pointing-directions within the same redshift limit (Figure 2, right) and a total of  $\sim 18,400$  sources in an individual simulation within the extrapolated distance of  $z \leq 0.2$ .

The simulated isotropic pointing-direction FR0s match the redshift distance distribution of data shown in Figure 3a, therefore the overall spatial distribution is not exactly volumetrically isotropic. The relative emission flux distribution is proportional to the radio output distribution (Figure 3b). Furthermore, the simulated FR0s preserve the correlation between radio (a source jet power measure)/UHECR flux and redshift (Figure 3c) to model the local universe source evolution.

As this method is probabilistic based on observational FR0 data, it is more realistic than the usual functional source evolution form used for combined fits of  $(1+z)^m$  [37, 38, 39]. A fit to the emissivity versus redshift to this functional form results in  $m = -31$ . The cosmology used to convert FR0 catalog redshifts to distance was the Planck 2015 results [40].

The UHECR flux of each simulated FR0 source is emitted isotropically. The isotropic emission model for FR0s is based on their morphological characteristics approximating that they appear to possess relatively slow bulk flows, which suggest a lack of strong directional biases in their emissions. To refine our understanding of FR0 contributions, future work may explore anisotropic emission scenarios using emission cones and pointing-directions, assessing their impacts on UHECR propagation and detection.

### 4.1. Simulated Energy Spectrum

The simulated UHECR emission energies are a uniform distribution following an  $E_0^{-1}$  energy spectrum for  $10^{18.6} \leq E/\text{eV} < 10^{20.2}$ . This spectrum is modified by interactions in the intergalactic medium during propagation to the observer, as demonstrated for the case with no

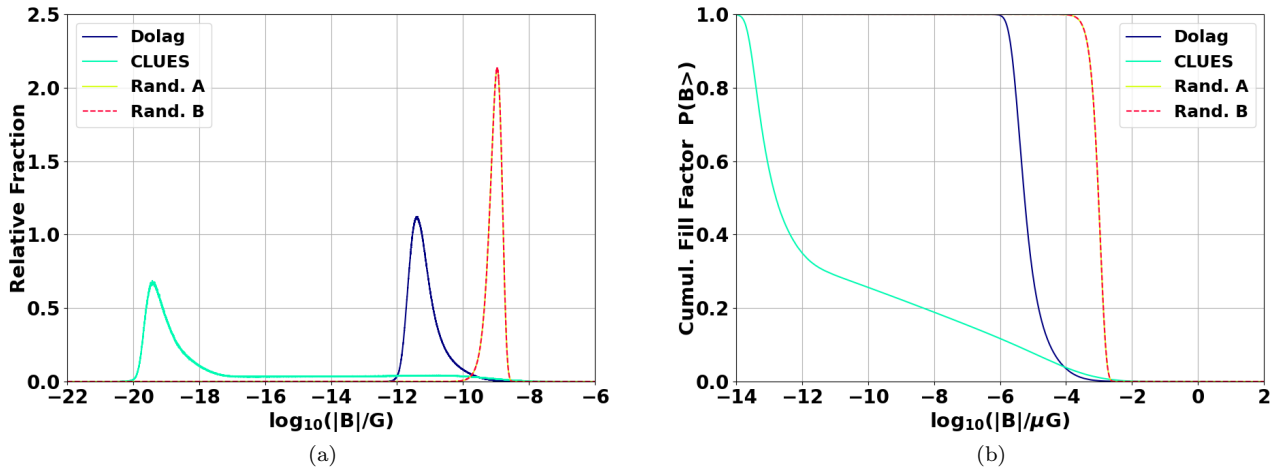


Figure 1: Magnetic field magnitude relative fraction and inverse cumulative distribution (or filling factor) of the simulated intergalactic magnetic field models used. The structured fields Dolag et al. ( $\langle B \rangle = 0.047$  nG,  $B_{\text{RMS}} = 11$  nG) [22] and Hackstein et al. (CLUES) ‘astrophysical1R’ ( $\langle B \rangle = 0.064$  nG,  $B_{\text{RMS}} = 1.2$  nG) [23], Random  $\langle B \rangle = 1$  nG fields with  $l_{\text{corr}} = 234$  kpc (Rand.A) and  $l_{\text{corr}} = 647$  kpc (Rand.B). The two random fields cannot be distinguished in this figure.

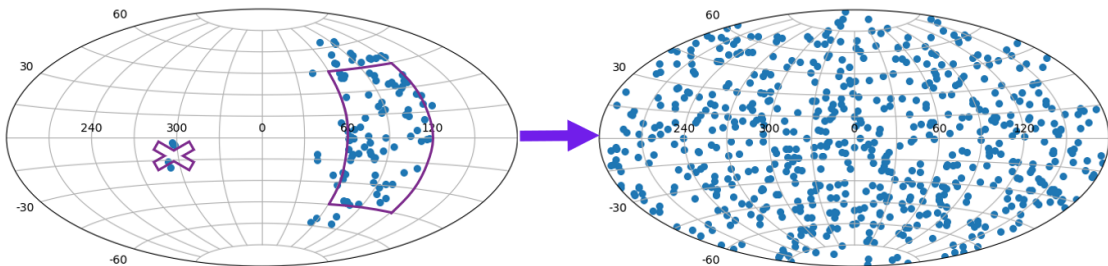


Figure 2: The FR0 catalog FR0CAT [3] in supergalactic coordinates (left) and a simulated FR0 distribution (right). Full-sky isotropic FR0 density is estimated from the well-sampled FR0CAT section. The crossed out FR0 on the left figure were not used in the fits shown in Figure 3

magnetic field and an unmodified  $E_0^{-1}$  emission spectrum in Figure 4. This propagated spectrum is modified when fitting to data by weighting the individual detected nuclei.

#### 4.2. Emitted Nuclei

Combined fits to the energy spectrum and estimated mean log mass number ( $\langle \ln A \rangle$ ) of data are done using sets of emitted proton, helium, nitrogen, silicon, and iron nuclei. These nuclei are commonly chosen in combined fit analyses as each elemental species can be considered as a family of neighboring nuclei and this selection represents a comprehensive sampling of cosmic ray nuclei observed in composition spectra. Studies suggest that heavier nuclei can originate from specific types of astrophysical environments, such as the dense, magnetized surroundings of AGN and elements heavier than iron should be rare enough to have a negligible impact on combined fits.

The emitted nuclei propagation is modeled according to their interaction cross-section with the photon fields, energy loss due to radiation emission, and deflection by cosmic magnetic fields as described in Section 3, and are modified by the time they are observed. The resulting combined fit  $\langle \ln A \rangle$  in bins of observed energy is shown in Figure 5 for an example configuration and illustrates how different nuclei are modified from emission to detection. The observed  $\langle \ln A \rangle$  slightly varies between the fitted configurations depending on the energy spectrum fit parameters spectral index  $\gamma$ , rigidity-dependent exponential cutoff  $R_{\text{cut}}$ , and trajectory cutoff  $D_{\text{cut}}$ . Emitted proton is, of course, unmodified and has a  $\langle \ln A \rangle = 0$ . The emitted nuclei resulting observed  $\langle \ln A \rangle$  for all evolving fraction fits (see Section 5.2) is shown in Appendix A.

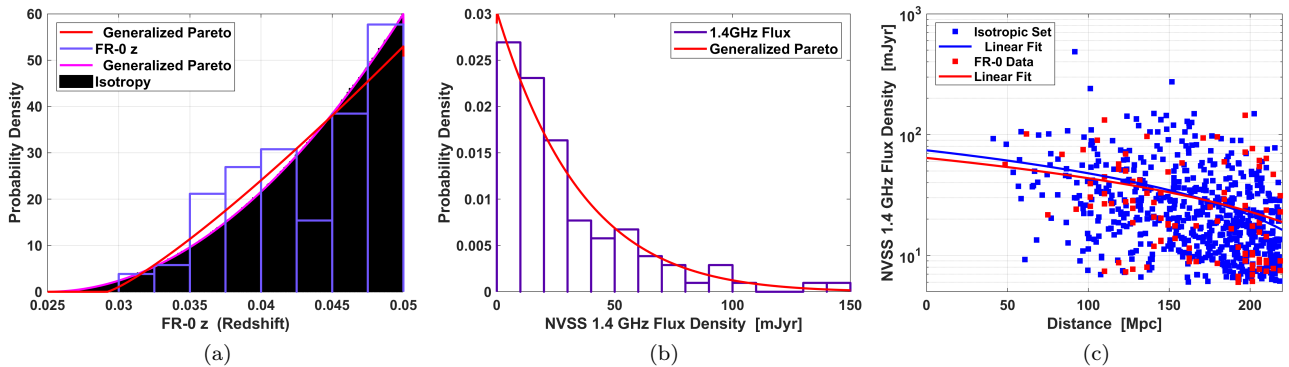


Figure 3: (a) A Pareto distribution fit to the catalog data [3] generates simulated FR0 redshifts. There is a  $\sim 16\%$  probability that FR0s are volumetrically isotropic. (b) Relative simulated FR0 UHECR flux is proportional to radio output distribution. Generated by Pareto distribution fit to NVSS data (p-value deviation from Gaussian:  $3.5 \times 10^{-9}$ ) [3]. (c) Local universe source evolution modeled by preserving the redshift/flux correlation (Kendall's correlation coefficient:  $-0.28$ , p-value:  $4.6 \times 10^{-5}$ ) from [3].

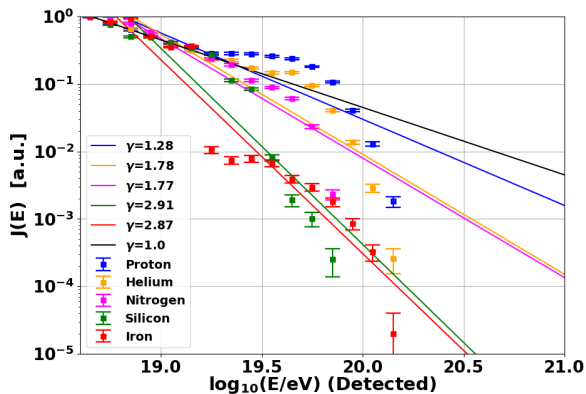


Figure 4: Relative energy spectra (maximum normalized to one) of simulations modified from the thrown/emitted  $E_0^{-1}$  spectrum after intergalactic propagation. Shown are sets of nuclei that were initially proton, helium, nitrogen, silicon, and iron in the case with no intergalactic magnetic fields. Simple linear fits are shown to compare to the thrown  $\gamma = -1$ .

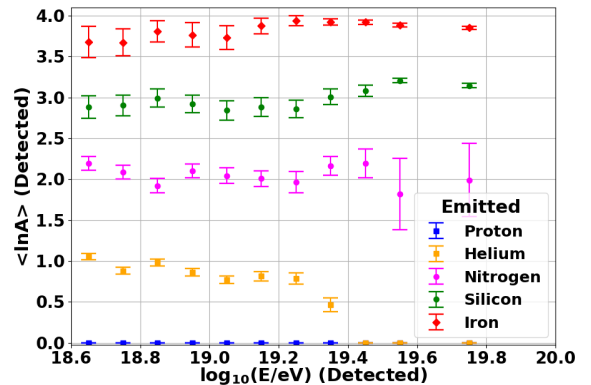


Figure 5: Emitted nuclei interact with the simulated intergalactic medium and are modified before observation. Shown are the emitted nuclei observed  $\langle \ln A \rangle$  for the constant energy-independent nuclei fraction best-fit configuration CLUES-SIBYLL.

## 5. Combined Fit of Composition and Energy Spectrum

### 5.1. Constant Fraction Fits

For the constant energy-independent observed fraction fit, the simulated FR0 UHECR emission that best matches Auger data [27, 28] is found by minimizing the summed  $\chi^2$  per degree of freedom for the composition and energy spectrum, considering eight input parameters. This fitting process utilizes four parameters representing the fractions of emitted protons, helium, nitrogen, silicon, and iron. These fractions, spanning the entire energy spectrum, are constrained to sum to 100%. The remaining parameters include the emitted spectral index  $\gamma$ , rigidity-dependent exponential cutoff  $R_{\text{cut}}$  [37, 38, 39], maximum particle trajectory cutoff  $D_{\text{cut}}$ , and energy spectrum normalization  $n$ .

The total cost function minimized is the sum of the  $\chi^2$  per degree-of-freedom for composition and energy spectrum comparisons between simulation and data:

$$\sum \chi^2 / N_{\text{dof}} = \sum \chi_E^2 / N_{\text{dof}}^E + \sum \chi_C^2 / N_{\text{dof}}^C. \quad (1)$$

For the sake of uniformity of our analysis, the accompanying variance of  $\ln A$  ( $\text{Var}(\ln A)$ ) was not used in this work due to the unphysical negative values calculated for the QGS4 hadronic interaction model [27, 29]. A different method to find  $\text{Var}(\ln A)$  was also reported in [27] using the correlation between  $X_{\text{max}}$  and a variable proportional to EAS muon content ( $S_{38}$ ) for the same three EAS models used in the present work [41]. The resulting variances are given for one energy bin ( $10^{18.5} \leq E/\text{eV} \leq 10^{19.0}$ ) as  $\text{Var}(\ln A) \approx 1.64 \pm 0.92$  — this does not include uncertainty from the fact that EAS models do not adequately account for muons [42, 43]. The result is not a strong constraint and allows a wide range of UHECR nuclei composition mixes.

To minimize Equation 1, the SciPy optimization library [44] is employed. The process involves an initial global minimization using stochastic Differential Evolution [45], followed by a refined deterministic local search to ensure precise fitting. Finally, a repeated deterministic nested fit is done, holding the spectrum parameters constant while varying the elemental content found in the previous step and vice versa.

This search method allows for a comprehensive exploration of the parameter space. The search limits include: spectral index  $-4.5 \leq \gamma \leq 4.5$  ( $E^{-\gamma}$ ), rigidity-dependent cutoff  $10^{16} \leq R_{\text{cut}}/V \leq 10^{22}$ , and maximum particle trajectory cutoff  $841 \leq D_{\text{cut}}/\text{Mpc} \leq 2000$ . The large range of rigidity-dependent exponential cutoff effectively results in two alternate models tested for — (dominant) exponential emission and (almost) pure power law.

Uncertainties on the fit parameters are calculated as bootstrapped 68.27% confidence intervals ( $1\sigma$  Gaussian equivalent) around the best-fit values. The bootstrap samples include random sampling with replacement for the simulation outputs and random Gaussian perturbations to the data using the total systematic and statistical uncertainties. This way, uncertainties on the fitting method, simulation and data statistics, and systematic data uncertainties are considered. The result is conservative error bars on all fit parameters as bin-by-bin systematic correlations are unknown and not considered.

Generally, the data or bootstrap samples result in fits that do not reach the bounds of the parameters (except the Dolag-EPOS configuration bootstrap samples have some  $D_{\text{cut}} = 2000$  Mpc). However, the Dolag-SIBYLL configuration yielded a best-fit spectral index of  $\gamma = 0.5$ , leading to significantly suppressed photon and neutrino spectra. Given the variability in the Dolag-SIBYLL  $\gamma$  distribution across bootstrap samples, with the highest peak at  $\gamma = 2.29$ , the Dolag-SIBYLL spectral index is constrained to  $\gamma \geq 1.5$  to ensure physically reasonable photon/neutrino spectra.

### 5.2. Evolving Fraction Fit

For the evolving energy-dependent observed fraction fit, the simulated FR0 UHECR emission that best matches Auger data [27, 28] is found by minimizing the summed  $\chi^2$  per bin for the composition and energy spectrum. This approach involves forty-eight input parameters, providing a detailed, bin-specific analysis. Forty-four parameters represent the fractions of emitted protons, helium, nitrogen, silicon, and iron, calculated for each of the eleven energy bins used in the Auger composition data, with each bin's total fraction constrained to 100%. The remaining parameters are the same energy spectrum parameters as Section 5.1. Though an evolving nuclei fraction dependent on energy is not a good model discriminator due to overfitting, it is more capable of reflecting physical processes than a constant observed fraction model. This detailed modeling provides a deeper picture of the emission require-

ments for each EAS model and magnetic field for the best possible fit.

The cost function minimized is the sum of the  $\chi^2$  per bin for composition and energy spectrum comparisons between simulation and data and is minimized first using the constant fraction fit as an initial search value. The fitting process then iteratively refines the model by splitting element fractions into increasingly detailed energy ranges (two energy ranges, then four fractions, and finally eleven fractions, one for each energy bin), applying deterministic nested fitting at each step. As before the nested fitting holds the spectrum parameters constant while varying the elemental content found in the previous step then vice versa. Additional improvement of the result is done by a nested fit one energy bin at a time (keeping all others constant) and then a final fit of all 48 parameters at once.

As before, this method facilitates an extensive global search of possible values of the parameters, though given the results of the constant fraction fit  $\gamma$  can be more constrained to  $1 \leq \gamma \leq 3.5$  without a loss in bootstrap uncertainty calculation. Uncertainties on the fit parameters are calculated the same as Section 5.1.

## 6. Results

### 6.1. Constant Fraction Fit

The constant observed fraction combined fit results for all five simulated intergalactic media and two EAS models (EPOS-LHC and Sibyll2.3c) compared to Auger data [27, 28] are shown in Figure 6. Results for the QGS-JetII-04 model are detailed in subsequent tables. For the observed mean log mass number  $\langle \ln A \rangle$  (Figure 6a), the 1nG random fields show a better fit for the lower energy, lighter composition, bins. In contrast, only the Dolag and Rand.B models sufficiently account for the data in the highest energy bin of the energy spectrum, as shown in Figure 6b — though the Dolag model overshoots the previous two bins. The excellent fit of the longer correlation length 1 nG (Rand.B) field at the highest energies is somewhat unexpected, if FR0s do not contribute significantly at these extreme energies. The CLUES model, being on the order of  $J(E) * E^3 \sim 10^{33} \text{ eV}^2 \text{ km}^{-2} \text{ yr}^{-1} \text{ str}^{-1}$ , essentially does not contribute to the highest energy bin.

Table 1 and Table 3 detail the best-fit parameters for each model configuration, along with the corresponding  $1\sigma$  equivalent confidence intervals that provide a measure of the uncertainty around these estimates. Using an 8-dimensional multivariate (all fit parameters) kernel density estimation (KDE), Table 2 and Table 4 present the most probable values and  $1\sigma$  standard deviations derived from the bootstrap sample distributions.

Table 1 and Table 2 show each EAS model and magnetic field's total  $\Sigma\chi^2/\text{dof}$ , emission spectral index ( $\gamma$ ), exponential rigidity-dependent cutoff ( $\log_{10}(R_{\text{cut}})$ ), particle trajectory cutoff ( $D_{\text{cut}}$ ), and relative energy spectrum normalization ( $n$ ). Table 3 and Table 4 show the fitted FR0 emission elemental fractions.

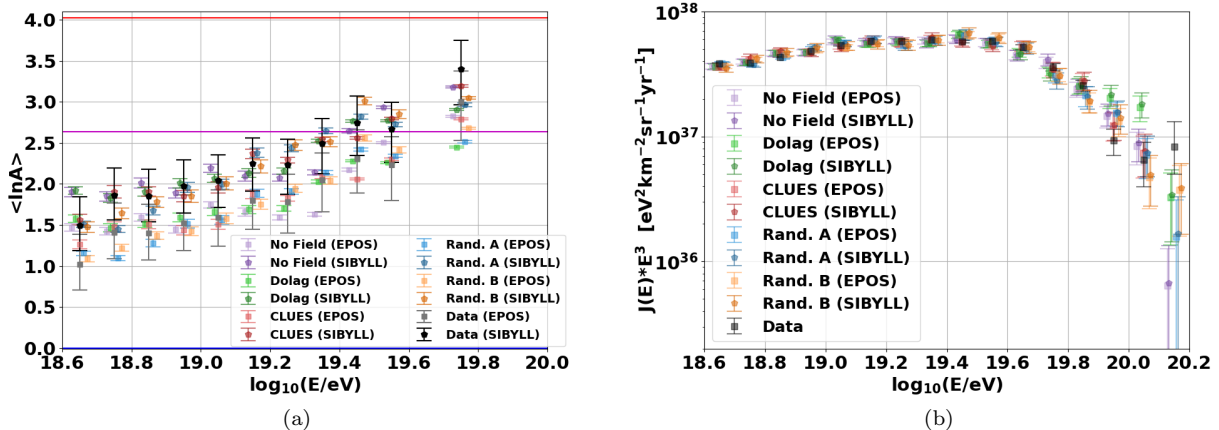


Figure 6: Constant fraction combined fit results for all simulated magnetic fields and two EAS models (EPOS-LHC (EPOS) and Sibyll2.3c (SIBYLL)) compared to Auger data [27, 28]. The data error bars include statistical and systematic uncertainties. Slight offsets are applied in the x-axis for improved visibility. (a) Mean log mass number  $\langle \ln A \rangle$ . Horizontal lines are blue:proton, magenta:nitrogen, and red:iron. (b) Energy spectra multiplied by  $E^3$  for visibility.

Table 1 shows that the magnetic fields CLUES, Rand.A, and Rand.B generally exhibit the best fits. Specifically, the CLUES magnetic field yields the best fit for the EPOS-LHC and Sibyll2.3c EAS models, while the Rand.A field is optimal for the QGSJetII-04 model. The CLUES-SIBYLL configuration is the overall best fit, closely followed by CLUES-EPOS. Additionally, the EPOS-LHC model performs well paired with either random field model, demonstrating a robustness across different magnetic environments. When considering only EPOS and SIBYLL, the second-best magnetic field after CLUES is Rand.B.

Models with minimal magnetic fields, such as the 'no-field' or Dolag scenarios, are disfavored for all three EAS models, indicating a significant influence of magnetic fields on fit accuracy. Notably, the QGSJetII-04 EAS model typically shows a much poorer fit quality compared to the others, except when combined with the random fields, suggesting a sensitivity to specific intergalactic conditions.

### 6.1.1. Energy Spectrum Parameters

Analysis of the constant fraction energy spectrum parameters of Table 1 and Table 2 suggest that both the magnetic field strength ( $B$ ) and RMS  $B_{\text{RMS}}$  influence the expected cosmic-ray source emission energy spectrum. However, the results are perhaps surprisingly stable given the wide range of magnetic field models and EAS model compositions. As  $\langle B \rangle$  or  $B_{\text{RMS}}$  increases, the emission spectral index  $\gamma$  does decrease – with generally harder emission spectra for QGSJetII-04. The fit values of the exponential rigidity-dependent cutoff,  $\log_{10}(R_{\text{cut}})$ , generally increases with both  $\langle B \rangle$  and  $B_{\text{RMS}}$ . For smaller magnetic fields, the rigidity cutoff decreases with a heavier elemental composition, while it increases with larger field strengths. The trajectory cutoff fit values,  $D_{\text{cut}}$ , remain fairly consistent across the fields tested, with the exception of the Dolag

field, where a significantly higher  $B_{\text{RMS}}$  of 11 nG introduces a noticeable deviation.

Also, for any given magnetic field, EAS models that result in a heavier composition  $\langle \ln A \rangle$  (Sibyll2.3c is heaviest  $\langle \ln A \rangle$  as shown in Figure 6a and QGSJetII-04 is the lightest  $\langle \ln A \rangle$ ) leads to a softer (increasing) spectral index  $E^{-\gamma}$ . An exception occurs with the bootstrap KDE most probable  $\gamma$  for Dolag-SIBYLL shown in Table 2, as this configuration fit leads to multi-modal distributions (a 1-d KDE fit results in  $\gamma=2.30$ ).

Compared to the previous FR0 combined fit results, with sources limited to  $z \leq 0.05$  (and a slightly older CR-Propa version), the emission spectra for the QGSJetII-04 and EPOS-LHC EAS models are harder (a smaller  $\gamma$ ). The exponential cutoff has also increased for all scenarios, with the exception of the Rand.B magnetic field [24].

Excluding the disfavored magnetic fields (no-field and Dolag) and the disfavored CLUES-QGS4 configuration, the bounds found for the best fit of these parameters from Table 1 are:

- $1.97 \leq \gamma \leq 2.54$
- $19.45 \leq \log_{10}(R_{\text{cut}}/V) \leq 19.86$
- $842 \text{ Mpc} \leq D_{\text{cut}} \leq 854 \text{ Mpc}$
- $1.341 \leq n \leq 1.354$

For the bootstrap most probable parameters from Table 2, excluding the disfavored configurations, the ranges found are:

- $2.15 \leq \gamma \leq 2.54$
- $19.41 \leq \log_{10}(R_{\text{cut}}/V) \leq 19.87$
- $842 \text{ Mpc} \leq D_{\text{cut}} \leq 864 \text{ Mpc}$

Constant Fraction Energy Spectrum Parameters

Field	Model	$\Sigma\chi^2/\text{dof}$	$\gamma$	$\log_{10}(\mathbf{R}_{\text{cut}}/V)$	$\mathbf{D}_{\text{cut}}/\text{Mpc}$	$\mathbf{n}$
No Field	SIBYLL	3.21	$2.51^{+0.02}_{-0.67}$	$19.36^{+0.23}_{-0.31}$	$843^{+0}_{-0}$	$1.337^{+0.016}_{-0.003}$
	EPOS	3.15	$2.50^{+0.02}_{-0.16}$	$19.40^{+0.13}_{-0.06}$	$843^{+0}_{-0}$	$1.337^{+0.011}_{-0.004}$
	QGS4	3.47	$2.47^{+0.03}_{-0.08}$	$19.43^{+0.10}_{-0.03}$	$843^{+0}_{-0}$	$1.338^{+0.006}_{-0.006}$
Dolag	SIBYLL	4.41	$2.29^{+0.06}_{-0.79}$	$19.74^{+0.00}_{-0.40}$	$890^{+320}_{-41}$	$1.341^{+0.008}_{-0.008}$
	EPOS	4.74	$2.23^{+0.11}_{-0.06}$	$19.75^{+0.03}_{-0.29}$	$889^{+230}_{-41}$	$1.339^{+0.007}_{-0.007}$
	QGS4	6.28	$2.23^{+0.08}_{-0.09}$	$19.64^{+0.10}_{-0.12}$	$890^{+47}_{-42}$	$1.335^{+0.005}_{-0.008}$
CLUES	SIBYLL	1.76	$2.54^{+0.00}_{-0.19}$	$19.45^{+0.50}_{-0.12}$	$842^{+0}_{-0}$	$1.354^{+0.006}_{-0.015}$
	EPOS	1.87	$2.43^{+0.06}_{-0.13}$	$19.51^{+0.36}_{-0.07}$	$842^{+0}_{-1}$	$1.347^{+0.006}_{-0.011}$
	QGS4	3.10	$2.32^{+0.08}_{-0.05}$	$19.56^{+0.08}_{-0.07}$	$841^{+1}_{-0}$	$1.334^{+0.006}_{-0.007}$
Rand.A	SIBYLL	2.84	$2.40^{+0.07}_{-0.11}$	$19.86^{+0.12}_{-0.18}$	$843^{+80}_{-0}$	$1.342^{+0.007}_{-0.005}$
	EPOS	2.15	$2.34^{+0.08}_{-0.09}$	$19.69^{+0.19}_{-0.08}$	$843^{+76}_{-0}$	$1.341^{+0.006}_{-0.004}$
	QGS4	2.51	$2.23^{+0.07}_{-0.07}$	$19.58^{+0.07}_{-0.08}$	$846^{+69}_{-0}$	$1.341^{+0.005}_{-0.006}$
Rand.B	SIBYLL	2.57	$2.47^{+0.04}_{-0.16}$	$19.71^{+1.40}_{-0.08}$	$843^{+156}_{-0}$	$1.346^{+0.009}_{-0.006}$
	EPOS	2.29	$2.33^{+0.09}_{-0.15}$	$19.60^{+0.23}_{-0.09}$	$843^{+140}_{-0}$	$1.346^{+0.005}_{-0.006}$
	QGS4	2.60	$1.97^{+0.26}_{-0.05}$	$19.52^{+0.08}_{-0.07}$	$854^{+66}_{-11}$	$1.343^{+0.006}_{-0.004}$

Table 1: The FR0 constant fraction combined fit results total sum chi-square per degree of freedom, spectral index  $\gamma$ , exponential rigidity cutoff ( $\log_{10}(\mathbf{R}_{\text{cut}})$ ), trajectory cutoff ( $\mathbf{D}_{\text{cut}}$ ), and spectrum normalization for all 15 configurations. The three EAS models are EPOS-LHC (EPOS), Sibyll2.3c (SIBYLL), and QGSJetII-04 (QGS4).

- $1.342 \leq n \leq 1.352$

Compared to the recent Auger result of [37] these parameter values are similar to the reported second minima of their models and the low  $z$  source distance model ( $z < 0.02$ ).

### 6.1.2. UHECR Composition Parameters

The FR0 emission fractions for constant (observed) fraction fits of emitted proton, helium, nitrogen, silicon, and iron nuclei are given in Table 3, Table 4, and Figure 7. Due to significant propagation effects, where a large percentage of emitted helium transforms into observed protons (as detailed in Figure 5), the best fit emission fractions for protons and helium exhibit some degeneracy. This results in instability in determining whether protons or helium dominate for a given magnetic field. The combined light component fraction ( $f_{\text{H}} + f_{\text{He}}$ ) and the corresponding KDE most probable values of Table 4 show more stable results.

Table 3, Table 4, and Figure 7 display the emission fractions for protons, helium, nitrogen, silicon, and iron as part of the constant observed fraction fits of FR0 emitted nuclei. These results indicate that magnetic field strength can significantly impact the relative nuclei abundances of the source-emitted cosmic rays. As the magnetic field strength increases, the emission fractions of protons and helium remains relatively stable. In contrast, the fractions of nitrogen nuclei tend to increase, whereas heavier nuclei such as silicon and iron show a decrease in their relative fractions.

Compared to the previous FR0 combined fit results, with sources limited to  $z \leq 0.05$ , the helium fractions have significantly increased for the QGSJetII-04 and EPOS-LHC EAS models (except for the no-field scenario) [24]. The amount of proton has commensurately decreased for these configurations (except for the no-field scenario). Also, comparatively, there is now more nitrogen for the Rand.A-EPOS and Rand.B-EPOS configurations and less nitrogen for the Rand.A-QGS4 and Rand.B-QGS4 configurations. The fraction of silicon has decreased for all configurations except for a small increase for Rand.B-QGS4. Finally, the iron fraction has increased for all magnetic fields except for the no-field scenario [24].

Excluding the disfavored configurations, the ranges found for the FR0 emission best fit elemental fractions (in %) from Table 3 are:

- $58.4 \leq f_{\text{H}} + f_{\text{He}} \leq 98.9$
- $0.0 \leq f_{\text{H}} \leq 74.5$
- $10.1 \leq f_{\text{He}} \leq 69.3$
- $0.0 \leq f_{\text{N}} \leq 38.8$
- $0.0 \leq f_{\text{Si}} \leq 1.3$
- $1.1 \leq f_{\text{Fe}} \leq 8.2$

The analysis shows a broad range of elemental fractions, with the most notable being a substantial variation in the combined proton and helium fraction, ranging from 58.4% to 98.9%, and the fraction of nitrogen ranging from



Constant Fraction Bootstrap Energy Spectrum Parameters

Field	Model	$\Sigma\chi^2/\text{dof}$	$\gamma$	$\log_{10}(\mathbf{R}_{\text{cut}}/V)$	$\mathbf{D}_{\text{cut}}/\text{Mpc}$	$\mathbf{n}$
No Field	SIBYLL	3.21	$2.48^{+0.27}_{-0.27}$	$19.38^{+0.23}_{-0.23}$	$843^{+0}_{-0}$	$1.341^{+0.006}_{-0.006}$
	EPOS	3.15	$2.48^{+0.26}_{-0.26}$	$19.40^{+0.13}_{-0.13}$	$843^{+0}_{-0}$	$1.338^{+0.005}_{-0.005}$
	QGS4	3.47	$2.45^{+0.04}_{-0.04}$	$19.43^{+0.06}_{-0.06}$	$843^{+0}_{-0}$	$1.335^{+0.004}_{-0.004}$
Dolag	SIBYLL	4.41	$2.07^{+0.23}_{-0.23}$	$19.04^{+0.57}_{-0.57}$	$871^{+126}_{-29}$	$1.339^{+0.005}_{-0.005}$
	EPOS	4.74	$2.33^{+0.38}_{-0.38}$	$19.37^{+0.24}_{-0.24}$	$864^{+180}_{-22}$	$1.334^{+0.004}_{-0.004}$
	QGS4	6.28	$2.24^{+0.37}_{-0.37}$	$19.64^{+0.07}_{-0.07}$	$893^{+86}_{-51}$	$1.335^{+0.004}_{-0.004}$
CLUES	SIBYLL	1.76	$2.54^{+0.15}_{-0.15}$	$19.41^{+0.34}_{-0.34}$	$842^{+0}_{-0}$	$1.352^{+0.007}_{-0.007}$
	EPOS	1.87	$2.41^{+0.07}_{-0.07}$	$19.51^{+0.15}_{-0.15}$	$842^{+0}_{-0}$	$1.346^{+0.005}_{-0.005}$
	QGS4	3.10	$2.31^{+0.05}_{-0.05}$	$19.56^{+0.06}_{-0.06}$	$842^{+0}_{-0}$	$1.337^{+0.004}_{-0.004}$
Rand.A	SIBYLL	2.84	$2.36^{+0.26}_{-0.26}$	$19.87^{+1.66}_{-1.66}$	$864^{+81}_{-22}$	$1.343^{+0.001}_{-0.001}$
	EPOS	2.15	$2.31^{+0.05}_{-0.05}$	$19.67^{+0.11}_{-0.11}$	$853^{+36}_{-11}$	$1.343^{+0.003}_{-0.003}$
	QGS4	2.51	$2.25^{+0.07}_{-0.07}$	$19.59^{+0.08}_{-0.08}$	$854^{+29}_{-12}$	$1.342^{+0.004}_{-0.004}$
Rand.B	SIBYLL	2.57	$2.43^{+0.06}_{-0.06}$	$19.70^{+10.20}_{-10.20}$	$852^{+53}_{-10}$	$1.347^{+0.005}_{-0.005}$
	EPOS	2.29	$2.36^{+0.10}_{-0.10}$	$19.54^{+7.2}_{-7.2}$	$854^{+64}_{-12}$	$1.346^{+0.000}_{-0.000}$
	QGS4	2.60	$2.15^{+0.14}_{-0.14}$	$19.45^{+0.62}_{-0.62}$	$848^{+48}_{-6}$	$1.342^{+0.003}_{-0.003}$

 Table 2: The FR0 constant fraction combined fit bootstrap distribution most probable spectral index  $\gamma$ , exponential rigidity cutoff ( $\log_{10}(\mathbf{R}_{\text{cut}})$ ), trajectory cutoff ( $\mathbf{D}_{\text{cut}}$ ), and spectrum normalization for all 15 configurations.

zero to 38.8%. These ranges reflect the effect of interactions between magnetic fields and nuclei during cosmic ray propagation.

For the bootstrap most probable parameters from Table 4, excluding the disfavored configurations, the ranges found for the FR0 emission elemental fractions (%) are:

- $59.3 \leq f_{\text{H}} + f_{\text{He}} \leq 98.4$
- $5.3 \leq f_{\text{H}} \leq 81.2$
- $9.5 \leq f_{\text{He}} \leq 63.9$
- $0 \leq f_{\text{N}} \leq 35.8$
- $0 \leq f_{\text{Si}} \leq 0.7$
- $0.7 \leq f_{\text{Fe}} \leq 7.5$

It can be seen that the amount of silicon required is negligible for all configurations and its absence is not likely to affect the results significantly.

What may be expected from the constant fraction combined fits using the older Dominguez11 IR model is an increase in emitted helium and a decrease in proton with a hard emission spectrum – though this result could simply be due to fitting uncertainties [37, 38]. A more thorough comparison done in [46] with soft injection iron nuclei shows a smaller variation on the energy spectrum and a maximum 10% difference on  $\langle \ln A \rangle$  at  $10^{19.6}$  eV.

### 6.1.3. Multi-messenger Photons and Neutrinos

The constant fraction fit cosmogenic integral photon and all-flavor neutrino spectra are shown in Figures 8a

and 8b, respectively, for the best-fit configuration (compared to the no-field scenario) – the CLUES structured magnetic field and Sibyll2.3c-based mass composition. Although the Sibyll2.3c hadronic interaction model results in a heavier reconstructed mass for data compared to the other models, it predicts a 92% emission of light nuclei (protons and helium) from FR0 sources. At lower energies, the integral photon flux aligns closely with a theoretical prediction for a pure proton cosmogenic source, while at higher energies, it transitions into a range predicted for a mixed composition.

Notably, the neutrino flux resembles predictions for a pure iron source, a result that may be influenced by the simulation constraint to relatively proximate FR0 sources ( $z \leq 0.2$ ). However, although the previous FR0 combined fit results, limited to sources with  $z \leq 0.05$ , have fewer low-energy neutrinos and more high-energy neutrinos, the differences are not significant [24]. Considering the broad spectrum of theoretical predictions and current experimental upper limits, the simulated FR0 fluxes falls within a reasonable range. Overall, in both photon and neutrino spectra, the presence of a magnetic field generally leads to increased fluxes, with this effect being most pronounced at the highest energies, as shown in Figure 9.

### 6.2. Evolving Fraction Fits

The evolving fraction combined fit results for all five simulated intergalactic media and two EAS models (EPOS-LHC and Sibyll2.3c) compared to Auger data [27, 28] are shown in Figure 10. The QGSJetII-04 model was excluded from the evolving fraction analysis. The mean log mass number  $\langle \ln A \rangle$  shown in Figure 10a illustrates

Constant Fraction Composition Parameters

Field	Model	$f_{\text{H}}(\%) + f_{\text{He}}(\%)$	$f_{\text{H}}(\%)$	$f_{\text{He}}(\%)$	$f_{\text{N}}(\%)$	$f_{\text{Si}}(\%)$	$f_{\text{Fe}}(\%)$
No Field	SIBYLL	$88.7^{+0.2}_{-24.0}$	$88.7^{+0.1}_{-88.7}$	$0.0^{+16.5}_{-0.0}$	$0.0^{+23.1}_{-0.0}$	$6.1^{+6.8}_{-2.3}$	$5.2^{+2.0}_{-4.0}$
	EPOS	$93.4^{+0.7}_{-7.2}$	$93.4^{+0.6}_{-16.5}$	$0.0^{+12.1}_{-0.0}$	$0.0^{+5.8}_{-0.0}$	$2.9^{+2.4}_{-1.8}$	$3.7^{+0.8}_{-0.8}$
	QGS4	$97.6^{+0.3}_{-1.1}$	$97.6^{+0.1}_{-8.8}$	$0.0^{+7.8}_{-0.0}$	$0.0^{+0.0}_{-0.0}$	$0.2^{+1.2}_{-0.2}$	$2.2^{+0.2}_{-0.5}$
Dolag	SIBYLL	$84.3^{+5.2}_{-11.9}$	$0.0^{+85.6}_{-0.0}$	$84.3^{+0.0}_{-84.3}$	$0.0^{+16.6}_{-0.0}$	$2.5^{+10.5}_{-2.4}$	$13.2^{+0.0}_{-12.1}$
	EPOS	$90.8^{+3.7}_{-3.8}$	$0.0^{+87.9}_{-0.0}$	$90.8^{+0.0}_{-90.0}$	$0.0^{+0.0}_{-0.0}$	$0.0^{+5.8}_{-0.0}$	$9.2^{+0.0}_{-5.2}$
	QGS4	$97.1^{+0.4}_{-1.0}$	$54.4^{+28.3}_{-35.4}$	$42.7^{+34.7}_{-28.4}$	$0.0^{+0.0}_{-0.0}$	$0.0^{+0.0}_{-0.0}$	$2.9^{+0.9}_{-0.5}$
CLUES	SIBYLL	$91.8^{+0.3}_{-11.4}$	$74.5^{+8.5}_{-74.5}$	$17.3^{+66.2}_{-10.8}$	$0.0^{+0.0}_{-0.0}$	$0.0^{+9.2}_{-0.0}$	$8.2^{+3.5}_{-1.8}$
	EPOS	$94.4^{+0.4}_{-4.4}$	$68.6^{+14.1}_{-68.6}$	$25.8^{+64.4}_{-13.4}$	$0.0^{+0.0}_{-0.0}$	$0.0^{+3.5}_{-0.0}$	$5.6^{+0.9}_{-0.9}$
	QGS4	$97.4^{+0.4}_{-0.5}$	$68.8^{+16.3}_{-15.8}$	$28.6^{+15.6}_{-16.1}$	$0.0^{+0.0}_{-0.0}$	$0.0^{+0.0}_{-0.0}$	$2.6^{+0.5}_{-0.4}$
Rand.A	SIBYLL	$69.3^{+11.1}_{-19.2}$	$0.0^{+43.1}_{-0.0}$	$69.3^{+8.3}_{-54.4}$	$24.5^{+19.2}_{-12.3}$	$1.3^{+3.0}_{-1.3}$	$4.9^{+1.0}_{-1.4}$
	EPOS	$87.6^{+5.6}_{-4.2}$	$38.0^{+23.3}_{-38.0}$	$49.6^{+34.2}_{-23.5}$	$9.5^{+3.5}_{-7.3}$	$0.3^{+1.8}_{-0.3}$	$2.6^{+0.9}_{-0.5}$
	QGS4	$98.9^{+0.0}_{-3.5}$	$57.9^{+18.4}_{-12.1}$	$41.0^{+10.0}_{-20.7}$	$0.0^{+3.5}_{-0.0}$	$0.0^{+0.1}_{-0.0}$	$1.1^{+0.2}_{-0.2}$
Rand.B	SIBYLL	$58.4^{+10.5}_{-23.6}$	$48.3^{+5.3}_{-48.3}$	$10.1^{+41.8}_{-10.1}$	$38.8^{+22.2}_{-13.4}$	$0.0^{+3.5}_{-0.0}$	$2.8^{+1.6}_{-0.4}$
	EPOS	$79.5^{+5.8}_{-6.5}$	$57.7^{+20.2}_{-37.2}$	$21.8^{+34.9}_{-21.8}$	$18.2^{+5.8}_{-6.3}$	$0.7^{+1.9}_{-0.7}$	$1.6^{+0.7}_{-0.4}$
	QGS4	$95.8^{+1.7}_{-4.5}$	$45.6^{+41.0}_{-9.4}$	$50.2^{+9.0}_{-43.1}$	$2.2^{+5.1}_{-2.2}$	$0.9^{+0.6}_{-0.9}$	$1.1^{+0.2}_{-0.4}$

Table 3: The FR0 constant fraction combined fit nuclei emission percentages for proton, helium, nitrogen, silicon, and iron primaries for all 15 configurations.

that the inclusion of 44 nuclei fractions leads to a nearly perfect fit across all configurations due to the large number of parameters.

However, similar to the constant fraction fits 1 nG random fields results having a better fit to the (lnA) lower energy bins, these fields are the best fit to the two highest energy heavier bins with the evolving fractions. As with the constant fraction fits only the Rand.B configurations sufficiently account for the highest energy bin of the energy spectra as shown in Figure 10b. Continuing the trend observed in constant fraction fits, the superior performance of the longer correlation length 1 nG (Rand.B) field at the highest energies remains surprising, challenging the assumption that FR0s are minor contributors at extreme energies. And again, the CLUES model essentially does not contribute to the highest energy bin.

The best-fit parameters are presented in Table 5 and Figure 11, along with corresponding  $1\sigma$  equivalent confidence intervals around the best fit. Table 6 shows the most probable value of the bootstrap sample distributions using an four-dimensional multivariate kernel density estimation (KDE) and the  $1\sigma$  standard deviations of the KDEs. A 48-dimensional KDE estimation has not been done due to time and computing constraints and the 4D KDE should be a reasonable approximation.

For each EAS model and magnetic field, Table 5 and Table 6 show the total  $\Sigma\chi^2/\text{bin}$ , emission spectral index ( $\gamma$ ), exponential rigidity-dependent cutoff ( $\log_{10}(R_{\text{cut}})$ ), particle trajectory cutoff ( $D_{\text{cut}}$ ), and relative energy spectrum normalization ( $n$ ). Figure 11 shows the fitted FR0 emission elemental fractions as a function of energy for all 10 configurations.

As indicated in Table 5, similar to findings from constant fraction fits, the CLUES, Rand.A, and Rand.B magnetic fields consistently deliver the best fit results. The Rand.B field, in particular, does stand out as the optimal fit for both the EPOS-LHC and Sibyll2.3c models, with the Rand.B-SIBYLL configuration achieving the overall best fit (Rand.B-EPOS is a very close second). EPOS-LHC is the best fit for all magnetic field models except Rand.B-EPOS but the difference from SIBYLL is very small. The second-best magnetic field after Rand.B is CLUES.

### 6.2.1. Energy Spectrum Parameters

Overall, the evolving fraction fit energy spectrum parameters of Table 5 and Table 6 again indicate that both magnetic field strength ( $B$ ), and RMS  $B_{\text{RMS}}$ , have an impact on the expected cosmic-ray source emission energy spectrum. Generally, the emission spectral index,  $E^{-\gamma}$ , increases with the magnetic field strength ( $B$ ). However, the exception is the Rand.B field model where this trend does not apply. The exponential rigidity-dependent cutoff  $\log_{10}(R_{\text{cut}})$  generally rises with an increase in  $B_{\text{RMS}}$ , except in the case of the Rand.A field model. Furthermore, for smaller magnetic fields,  $\log_{10}(R_{\text{cut}})$  decreases with a heavier composition, while for larger fields, this trend is reversed, demonstrating the complex interaction between magnetic field strength and particle composition. The trajectory cutoff,  $D_{\text{cut}}$ , is fairly stable across most fields, with the notable exception of the Dolag field which has a significantly higher  $B_{\text{RMS}}$  of 11 nG.

Despite the no-field and Dolag configurations consistently showing poorer fits, similar to the constant fraction scenario, the inclusion of a large number of parameters in

Constant Fraction Bootstrap Composition Parameters

Field	Model	$f_H(\%) + f_{He}(\%)$	$f_H(\%)$	$f_{He}(\%)$	$f_N(\%)$	$f_{Si}(\%)$	$f_{Fe}(\%)$
No Field	SIBYLL	$86.3^{+13.7}_{-15.6}$	$85.6^{+14.4}_{-21.7}$	$0.6^{+15.2}_{-0.6}$	$2.8^{+15.8}_{-2.8}$	$5.6^{+3.1}_{-3.1}$	$5.4^{+2.3}_{-2.3}$
	EPOS	$92.8^{+5.3}_{-5.3}$	$91.4^{+8.6}_{-13.2}$	$1.4^{+10.7}_{-1.4}$	$0.6^{+5.3}_{-0.6}$	$2.9^{+1.5}_{-1.5}$	$3.7^{+0.8}_{-0.8}$
	QGS4	$97.6^{+0.8}_{-0.8}$	$96.4^{+3.6}_{-7.6}$	$1.2^{+7.4}_{-1.2}$	$0.0^{+0.8}_{-0.0}$	$0.2^{+0.5}_{-0.2}$	$2.2^{+0.2}_{-0.2}$
Dolag	SIBYLL	$85.2^{+8.0}_{-8.0}$	$84.4^{+15.6}_{-22.6}$	$0.9^{+22.1}_{-0.9}$	$0.0^{+7.6}_{-0.0}$	$13.0^{+3.9}_{-3.9}$	$1.8^{+3.1}_{-1.8}$
	EPOS	$94.8^{+4.9}_{-4.9}$	$84.5^{+15.5}_{-23.6}$	$10.3^{+22.4}_{-10.3}$	$0.1^{+4.7}_{-0.1}$	$0.2^{+2.2}_{-0.2}$	$4.9^{+1.7}_{-1.7}$
	QGS4	$97.0^{+0.6}_{-0.6}$	$54.7^{+18.0}_{-18.0}$	$42.3^{+17.7}_{-17.7}$	$0.0^{+0.5}_{-0.0}$	$0.0^{+0.3}_{-0.0}$	$2.9^{+0.5}_{-0.5}$
CLUES	SIBYLL	$91.6^{+3.6}_{-3.6}$	$81.2^{+18.8}_{-23.3}$	$10.6^{+20.7}_{-10.6}$	$0.0^{+2.2}_{-0.0}$	$0.7^{+3.4}_{-0.7}$	$7.5^{+1.9}_{-1.9}$
	EPOS	$94.2^{+1.8}_{-1.8}$	$66.7^{+21.8}_{-21.8}$	$27.6^{+20.5}_{-20.5}$	$0.0^{+0.5}_{-0.0}$	$0.2^{+1.6}_{-0.2}$	$5.5^{+1.0}_{-1.0}$
	QGS4	$97.5^{+0.4}_{-0.4}$	$67.6^{+12.3}_{-12.3}$	$29.9^{+12.1}_{-12.1}$	$0.0^{+0.0}_{-0.0}$	$0.0^{+0.2}_{-0.0}$	$2.5^{+0.3}_{-0.3}$
Rand.A	SIBYLL	$70.0^{+11.4}_{-11.4}$	$5.3^{+14.7}_{-5.3}$	$63.9^{+17.5}_{-17.5}$	$25.1^{+11.8}_{-11.8}$	$0.7^{+1.5}_{-0.7}$	$5.0^{+0.9}_{-0.9}$
	EPOS	$87.6^{+4.6}_{-4.6}$	$36.2^{+15.9}_{-15.9}$	$51.5^{+16.0}_{-16.0}$	$9.5^{+4.9}_{-4.9}$	$0.2^{+0.8}_{-0.2}$	$2.7^{+0.5}_{-0.5}$
	QGS4	$98.4^{+1.1}_{-1.1}$	$60.6^{+10.1}_{-10.1}$	$37.7^{+10.4}_{-10.4}$	$0.5^{+1.2}_{-0.5}$	$0.0^{+0.2}_{-0.0}$	$1.1^{+0.2}_{-0.2}$
Rand.B	SIBYLL	$59.3^{+11.1}_{-11.1}$	$45.7^{+15.3}_{-15.3}$	$15.2^{+14.4}_{-14.4}$	$35.8^{+11.5}_{-11.5}$	$0.6^{+1.3}_{-0.6}$	$2.7^{+0.6}_{-0.6}$
	EPOS	$82.0^{+4.5}_{-4.5}$	$73.3^{+16.3}_{-16.3}$	$9.5^{+14.8}_{-9.5}$	$15.6^{+4.7}_{-4.7}$	$0.2^{+1.0}_{-0.2}$	$1.4^{+0.4}_{-0.4}$
	QGS4	$93.6^{+1.8}_{-1.8}$	$80.4^{+14.2}_{-14.2}$	$13.2^{+14.7}_{-13.2}$	$5.6^{+2.1}_{-2.1}$	$0.0^{+0.4}_{-0.0}$	$0.7^{+0.2}_{-0.2}$

Table 4: The FR0 constant fraction combined fit bootstrap distribution most probable nuclei emission percentages for proton, helium, nitrogen, silicon, and iron primaries for all 15 configurations.

the evolving fraction fits leads to excellent overall fit quality for all configurations. Therefore, the bounds found for the best fit of these parameters from Table 1, using all configurations, are:

- $1.94 \leq \gamma \leq 2.65$
- $19.19 \leq \log_{10}(R_{\text{cut}}/V) \leq 19.95$
- $841 \text{ Mpc} \leq D_{\text{cut}} \leq 907 \text{ Mpc}$
- $1.328 \leq n \leq 1.346$

Note, that these bounds are larger than the constant fraction fit bounds due the inclusion of the no-field and Dolag configurations.

For the bootstrap KDE fit most probable parameters from Table 6 the ranges found are:

- $2.26 \leq \gamma \leq 2.47$
- $19.34 \leq \log_{10}(R_{\text{cut}}/V) \leq 19.83$
- $842 \text{ Mpc} \leq D_{\text{cut}} \leq 890 \text{ Mpc}$
- $1.335 \leq n \leq 1.348$

Compared to the recent Auger result of [37] these parameter values are similar to the reported second minima of their models and the low  $z$  source distance model ( $z < 0.02$ ).

### 6.2.2. UHECR Composition Parameters

The FR0 emission fractions for the evolving energy dependent (observed) fraction fit of proton, helium, nitrogen, silicon, and iron emitted nuclei are shown in Figure 11. Similar to the constant fraction fits, the emission fractions of protons and helium exhibit instability, with dominance of each varying due to propagation effects, as shown in Figure 5. The combined fraction of light components ( $f_H + f_{He}$ ) demonstrates greater stability across different configurations as shown in Figure 11f. Interestingly, for all configurations the fraction of emitted protons increases with energy above  $10^{19}$  eV as shown in Figure 11a.

These results suggest that the magnetic field strength can significantly impact the expected composition of the source-emitted cosmic rays, influencing the relative fractions of each element. With increasing magnetic field strength, the average emission percentages of protons and helium remain relatively stable. In contrast, the average fraction of nitrogen nuclei tends to increase, while heavier nuclei such as silicon and iron tend to decrease.

The ranges found for the energy bin average FR0 emission best fit elemental fractions (in %) from Figure 11 are:

- $63.3 \leq f_H + f_{He} \leq 95.0$
- $21.8 \leq f_H \leq 60.7$
- $27.0 \leq f_{He} \leq 52.6$
- $2.9 \leq f_N \leq 28.4$
- $1.1 \leq f_{Si} \leq 10.5$
- $0.6 \leq f_{Fe} \leq 6.4$

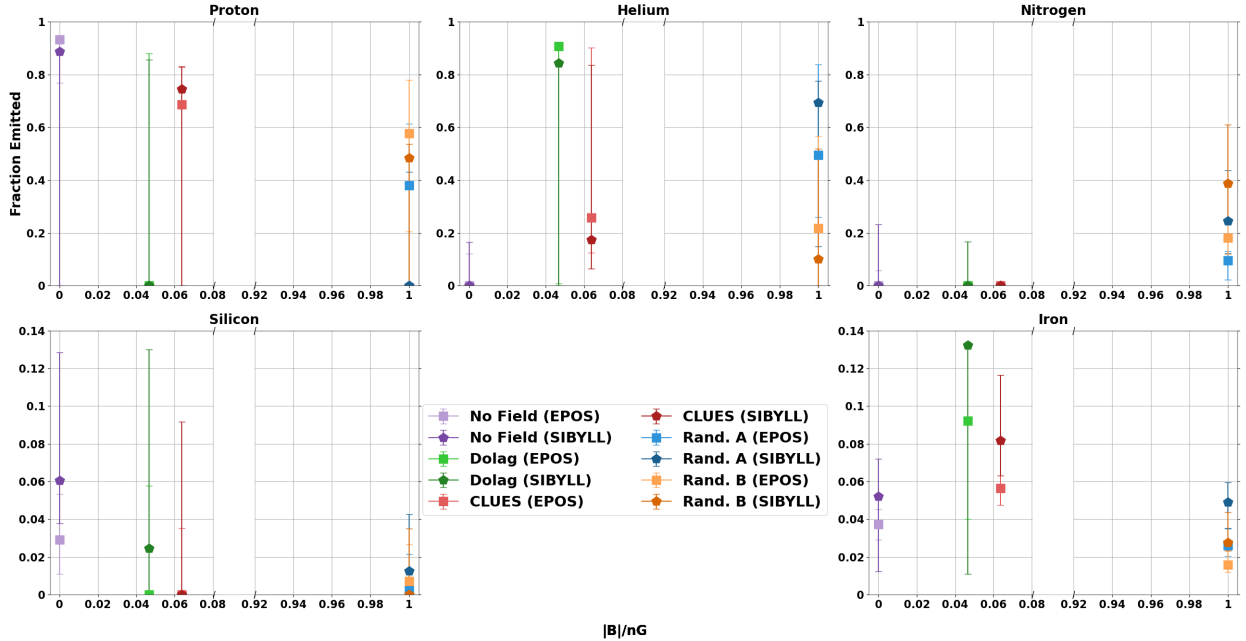


Figure 7: The constant observed fraction fit FR0 emitted nuclei fractions necessary to best fit the data for ten configurations based on the EPOS-LHC (EPOS) and Sibyll2.3c (SIBYLL) hadronic interaction models versus magnetic field strength. Note the different y-axis limits and the broken x-axis.

The observed ranges for average FR0 emission fractions across energy bins indicate that lighter elements like hydrogen and helium dominate, whereas it can be seen that the amount of heavier elements like iron contribute minimally for all configurations, and their absence is not likely to affect the results significantly.

As with the constant fraction fits Section 6.1.2, using the older Dominguez11 IR model may result in a small increase in emitted helium and a decrease in proton [37, 46, 38].

### 6.2.3. Multi-messenger Photons and Neutrinos

The evolving fraction fit cosmogenic integral photon and all-flavor neutrino spectra are shown in Figures 12a and 12b. These results are for the best-fit configuration using the Rand.B 1 nG random magnetic field and Sibyll2.3c-based mass composition, compared to the no-field scenario. Although the Sibyll2.3c hadronic interaction model reconstructs a heavier mass for data relative to other models, the evolving fraction fit still predicts that approximately 66% of the FR0 emission consists of light nuclei.

At lower energies (up to  $E_\gamma \leq 10^{17}$  eV), the integral photon flux is compatible with pure proton cosmogenic predictions, shifting towards a theoretical mixed composition at higher energies. Interestingly, the neutrino flux resembles predictions for a pure iron prediction, which may be partially influenced by the simulation constraint of relatively close FR0 sources ( $z \leq 0.2$ ). Given the wide range of theoretical predictions and current experimental upper limits the FR0 simulated flux is reasonable. Overall, for both photon and neutrino spectra, it can be seen that a

magnetic field results in a larger flux, particularly at higher energies, as shown in Figure 13.

## 7. Summary & Conclusions

This work presents an in-depth study of FR0 radio galaxies, a prevalent but less luminous class of jetted active galaxies, and their potential emission features as ultra-high-energy cosmic ray (UHECR) sources. Although individually less luminous than more powerful radio galaxies, the abundance of FR0 galaxies may render them significant contributors to the UHECR energy density observed on Earth.

To investigate this hypothesis, extensive CRPropa3 [26] simulations were conducted, modeling isotropic cosmic ray emissions extrapolated from measured FR0 properties (density and luminosity distributions and luminosity-redshift source evolution). These simulations were then fit to the mass composition (expressed in mean log mass number  $\langle \ln A \rangle$ ) and energy spectra of UHECR data from the Pierre Auger Observatory [27, 28].

The results from these combined fits, utilizing two fit models, three EAS models, and five intergalactic magnetic field configurations (both random and structured), indicate that emissions from FR0 galaxies can effectively account for the observed UHECR energy spectrum and composition. The overall compatibility, in addition to the results of our previous study of the capability of FR0 radio galaxies to accelerate cosmic rays up to ultra-high energies [6], supports the viability of FR0s as significant contributors to the observed UHECR flux. Furthermore,

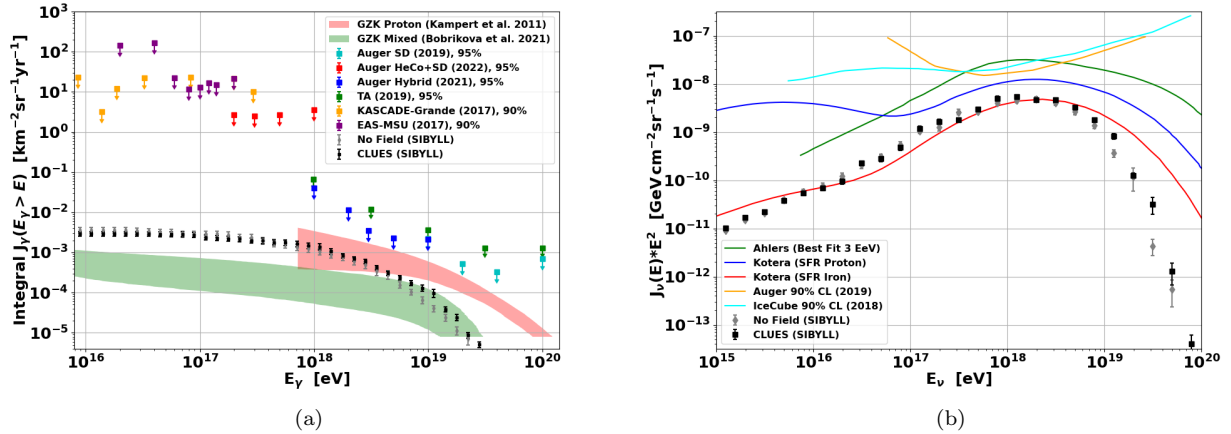


Figure 8: Constant fraction fit cosmogenic photon and neutrino spectra for the best fit CLUES-SIBYLL configuration (in black) compared to the no-field case (in grey). (a) Integral cosmogenic photon spectrum compared with two theoretical models and experimental upper limits as in [47]. (b) All-flavor neutrino spectrum compared with three theoretical models and experimental upper limits [48, 49, 50].

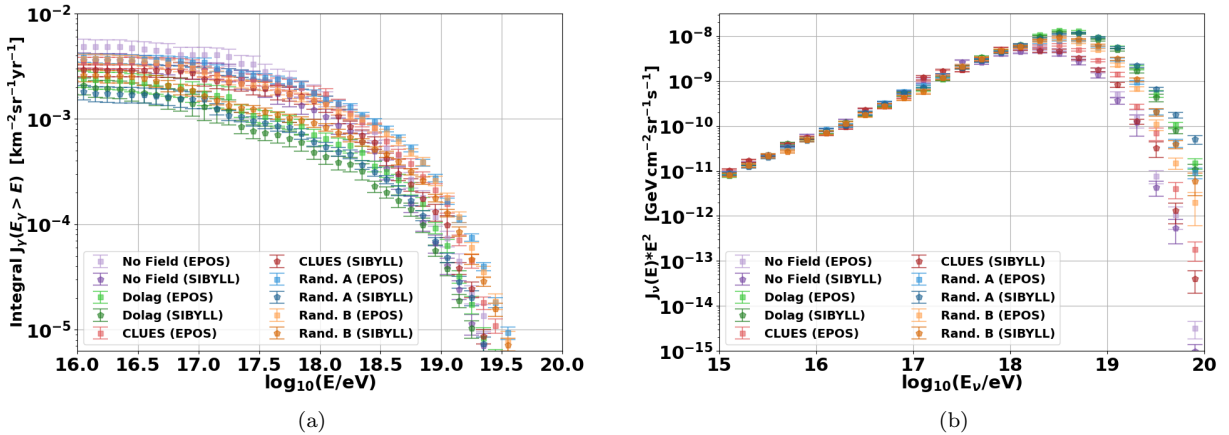


Figure 9: Constant fraction fit cosmogenic photon and neutrino spectra for the ten configurations based on EPOS-LHC (EPOS) and Sibyll2.3c (SIBYLL) hadronic interaction models. (a) Integral cosmogenic photon spectra. (b) All-flavor neutrino spectra multiplied by  $E^2$ .

the secondary photon and neutrino fluxes predicted from UHECR interactions are well within current observational limits, emphasizing the potential of future multi-messenger observations to further refine our understanding of FR0 galaxies as UHECR sources.

For the most extreme energy bin, the configurations tested are generally below the expected flux (only Dolag and *longer* correlation length 1 nG Rand.B magnetic field models have *overlapping* error bars, as shown in Figure 6b). Additionally, over all configurations, there is a small underfitting of the last energy bin of  $\langle \ln A \rangle$  (only Dolag and the *smaller* correlation length 1 nG Rand.A magnetic field models are *outside* the error bars as shown in Figure 6a). These two results may allow the possibility of a different extreme-energy heavy nuclei source type to become the dominant UHECR flux contributor.

These findings underscore the importance of consider-

ing the effects of intergalactic magnetic fields on UHECR propagation. Results across different magnetic field models indicate their significant influence on the arrival energy spectrum and composition of cosmic rays from FR0 galaxies, as well as on resulting secondary photon and neutrino spectra. Larger magnetic fields result in a greater emission of nuclei heavier than helium - additionally, generally, slightly harder emission spectra ( $\langle \gamma \rangle \approx 2.4$  compatible with Fermi shock acceleration), higher energy exponential cut-offs ( $\langle \log_{10}(R_{\text{cut}}/V) \rangle \approx 19.6$ ), and an increase in the highest energy secondary photons and neutrinos. The impact of magnetic field strength on light nuclei emission is the greatest for the more modern Sibyll2.3c and EPOS-LHC hadronic interaction models.

The Hackstein et al. (CLUES) 'astrophysical1R' model [23], characterized by  $\langle B \rangle = 0.064$  nG and  $B_{\text{RMS}} = 1.2$  nG, emerged as the best fit magnetic field model for

the constant nuclei fraction fits. This is compatible with a previous estimate in [51] of extragalactic magnetic fields using detected cosmic ray multiplets. Using the given  $\langle Z^*B^*D \rangle = 30 \text{ nG}^*\text{Mpc}$  (found with a mean energy cut of  $E \geq 27.7 \text{ EeV}$ ), the magnetic field of  $\langle B \rangle = 0.064 \text{ nG}$ , and the CLUES-SIBYLL best fit composition ( $\langle Z \rangle \approx 2.7$ ) results in an average particle trajectory length of about  $1.7 \times 10^2 \text{ Mpc}$ . Using the energy cut  $E \geq 27.7 \text{ EeV}$  from [51] and the CLUES-SIBYLL best-fit composition, the mean trajectory length of simulated particles is  $\sim 2.3 \times 10^2 \text{ Mpc}$ .

In conclusion, our comprehensive study provides strong evidence supporting the significant contribution of FR0 radio galaxies to the UHECR energy density. This work not only enhances our understanding of potential UHECR sources but also opens new avenues for multi-messenger astrophysics investigations.

## Acknowledgments

Financial support was received from the Austrian Science Fund (FWF) under grant agreement number I 4144-N27 and the Slovenian Research Agency - ARIS (project no. N1-0111). LM acknowledges support from the DFG within the Collaborative Research Center SFB1491 "Cosmic Interacting Matters - From Source to Signal". MB has for this project received funding from the European Union's Horizon 2020 research and innovation program under the Marie Skłodowska-Curie grant agreement No 847476. GB acknowledges financial support from the State Agency for Research of the Spanish MCIU through the "Center of Excellence Severo Ochoa" award to the Instituto de Astrofísica de Andalucía (SEV-2017-0709) and from the Spanish "Ministerio de Ciencia e Innovación" (MICINN) through grant PID2019-107847RB-C44. The views and opinions expressed herein do not necessarily reflect those of the European Commission. The Slovenian National Supercomputing Network provided extensive computing support.

## References

- [1] Aab, A., et al., The Pierre Auger Cosmic Ray Observatory, *Nucl. Instrum. Meth. A* 798 (2015) 172–213. [arXiv:1502.01323](#), [doi:10.1016/j.nima.2015.06.058](#).
- [2] Baldi, R.D., Capetti, A., Radio and spectroscopic properties of miniature radio galaxies: revealing the bulk of the radio-loud AGN population, *Astron. and Astrophys.* 508 (2) (2009) 603–614. [arXiv:0910.4261](#), [doi:10.1051/0004-6361/200913021](#).
- [3] Baldi, R.D., Capetti, A., Massaro, F., FR0CAT: a FIRST catalog of FR 0 radio galaxies, *Astron. Astrophys.* 609 (2018) A1. [arXiv:1709.00015](#), [doi:10.1051/0004-6361/201731333](#).
- [4] Croston, J.H., Ineson, J., Hardcastle, M.J., Particle content, radio-galaxy morphology, and jet power: all radio-loud AGN are not equal, *Mon. Not. R. Astron. Soc.* 476 (2) (2018) 1614–1623. [arXiv:1801.10172](#), [doi:10.1093/mnras/sty274](#).
- [5] Heckman, T.M., Best, P.N., The Coevolution of Galaxies and Supermassive Black Holes: Insights from Surveys of the Contemporary Universe, *Annu. Rev. Astron. Astrophys.* 52 (2014) 589–660. [arXiv:1403.4620](#), [doi:10.1146/annurev-astro-081913-035722](#).
- [6] Merten, L., et al., Scrutinizing FR0 radio galaxies as ultra-high-energy cosmic ray source candidates, *Astropart. Phys.* 128 (2021) 102564. [arXiv:2102.01087](#), [doi:10.1016/j.astropartphys.2021.102564](#).
- [7] Hillas, A.M., The Origin of Ultra-High-Energy Cosmic Rays, *Annu. Rev. Astron. Astrophys.* 22 (1984) 425–444. [doi:10.1146/annurev.aa.22.090184.002233](#).
- [8] Nagano, M., Watson, A.A., Observations and implications of the ultrahigh-energy cosmic rays, *Rev. Mod. Phys.* 72 (3) (2000) 689–732. [doi:10.1103/RevModPhys.72.689](#).
- [9] Bhattacharjee, P., Sigl, G., Origin and propagation of extremely high energy cosmic rays, *Phys. Rep.* 327 (2000) 109–247. [arXiv:astro-ph/9811011](#), [doi:10.1016/S0370-1573\(99\)00101-5](#).
- [10] Boughelilba, M., Reimer, A., On the Subparsec-scale Core Composition of FR 0 Radio Galaxies, *Astrophys. J. Lett.* 955 (2) (2023) L41. [arXiv:2310.06398](#), [doi:10.3847/2041-8213/acf83c](#).
- [11] Reimer, A., Boughelilba, M., Merten, L., Da Vela, P., Low-luminosity jetted AGN as particle multi-messenger sources, *PoS TAUP2023* (2024) 119. [doi:10.22323/1.441.0119](#).
- [12] Paliya, V.S., A New Gamma-Ray-emitting Population of FR0 Radio Galaxies, *Astrophys. J. Lett.* 918 (2) (2021) L39. [arXiv:2108.11701](#), [doi:10.3847/2041-8213/ac2143](#).
- [13] Khatiya, N.S., et al., Characterizing the  $\gamma$ -ray Emission from FR0 Radio Galaxies, *arXiv e-prints* [arXiv:2310.19888](#), [doi:10.48550/arXiv.2310.19888](#).
- [14] Partenheimer, A., Fang, K., Alves Batista, R., de Almeida, R.M., Ultra-high-energy Cosmic-Ray Sources Can Be Gamma-Ray Dim, *Astrophys. J. Lett.* 967 (1) (2024) L15. [arXiv:2404.17631](#), [doi:10.3847/2041-8213/ad4359](#).
- [15] Abdul Halim, A., et al., An update on the arrival direction studies made with data from the Pierre Auger Observatory, *PoS ICRC2023* (2023) 252. [doi:10.22323/1.444.0252](#).
- [16] Eichmann, B., et al., Ultra-high-energy cosmic rays from radio galaxies, *J. Cosmol. Astropart. Phys.* 2018 (2) (2018) 036. [arXiv:1701.06792](#), [doi:10.1088/1475-7516/2018/02/036](#).
- [17] Wittkowski, D., Kampert, K.H., On the Anisotropy in the Arrival Directions of Ultra-high-energy Cosmic Rays, *Astrophys. J. Lett.* 854 (1) (2018) L3. [arXiv:1710.05617](#), [doi:10.3847/2041-8213/aaa2f9](#).
- [18] Dundović, A., Sigl, G., Anisotropies of ultra-high energy cosmic rays dominated by a single source in the presence of deflections, *J. Cosmol. Astropart. Phys.* 2019 (1) (2019) 018. [arXiv:1710.05517](#), [doi:10.1088/1475-7516/2019/01/018](#).
- [19] Taylor, A.M., Ahlers, M., Hooper, D., Indications of negative evolution for the sources of the highest energy cosmic rays, *Phys. Rev. D* 92 (6) (2015) 063011. [arXiv:1505.06090](#), [doi:10.1103/PhysRevD.92.063011](#).
- [20] Das, S., Razzaque, S., Gupta, N., Ultrahigh energy cosmic rays and neutrinos from light nuclei composition, *Phys. Rev. D* 99 (8) (2019) 083015. [arXiv:1809.05321](#), [doi:10.1103/PhysRevD.99.083015](#).
- [21] Abdul Halim, A., et al., Constraining models for the origin of ultra-high-energy cosmic rays with a novel combined analysis of arrival directions, spectrum, and composition data measured at the Pierre Auger Observatory, *J. Cosmol. Astropart. Phys.* 01 (2024) 022. [arXiv:2305.16693](#), [doi:10.1088/1475-7516/2024/01/022](#).
- [22] Dolag, K., Grasso, D., Springel, V., Tkachev, I., Constrained simulations of the magnetic field in the local Universe and the propagation of ultrahigh energy cosmic rays, *J. Cosmol. Astropart. Phys.* 01 (2005) 009. [arXiv:astro-ph/0410419](#), [doi:10.1088/1475-7516/2005/01/009](#).
- [23] Hackstein, S., et al., Simulations of ultra-high energy cosmic rays in the local Universe and the origin of cosmic magnetic fields, *Mon. Not. Roy. Astron. Soc.* 475 (2) (2018) 2519–2529. [arXiv:1710.01353](#), [doi:10.1093/mnras/stx3354](#).
- [24] Lundquist, J.P., et al., The UHECR-FR0 Radio Galaxy Connection: A Multi-Messenger Study of Energy Spectra/Composition Emission and Extragalactic Magnetic Field Propagation, *PoS ICRC2023* (2023) 1512. [arXiv:2308.10803](#), [doi:10.22323/1.](#)

- 444.1512.
- [25] Mollerach, S., Roulet, E., Magnetic diffusion effects on the ultra-high energy cosmic ray spectrum and composition, *J. Cosmol. Astropart. Phys.* 10 (2013) 013. [arXiv:1305.6519](#), [doi:10.1088/1475-7516/2013/10/013](#).
- [26] Alves Batista, R., et al., CRPropa 3.2 — an advanced framework for high-energy particle propagation in extragalactic and galactic spaces, *J. Cosmol. Astropart. Phys.* 09 (2022) 035. [arXiv:2208.00107](#), [doi:10.1088/1475-7516/2022/09/035](#).
- [27] Yushkov, A., Mass Composition of Cosmic Rays with Energies above  $10^{17.2}$  eV from the Hybrid Data of the Pierre Auger Observatory, *PoS ICRC2019* (2020) 482. [doi:10.22323/1.358.0482](#).
- [28] Deligny, O., The energy spectrum of ultra-high energy cosmic rays measured at the Pierre Auger Observatory and at the Telescope Array, *PoS ICRC2019* (2020) 234. [arXiv:2001.08811](#), [doi:10.22323/1.358.0234](#).
- [29] Abreu, P., et al., Interpretation of the depths of maximum of extensive air showers measured by the Pierre Auger Observatory, *J. Cosmol. Astropart. Phys.* 02 (2013) 026. [arXiv:1301.6637](#), [doi:10.1088/1475-7516/2013/02/026](#).
- [30] Riehn, F., et al., The hadronic interaction model SIBYLL 2.3c and Feynman scaling, *PoS ICRC2017* (2018) 301. [arXiv:1709.07227](#), [doi:10.22323/1.301.0301](#).
- [31] Pierog, T., et al., EPOS LHC: Test of collective hadronization with data measured at the CERN Large Hadron Collider, *Phys. Rev. C* 92 (3) (2015) 034906. [arXiv:1306.0121](#), [doi:10.1103/PhysRevC.92.034906](#).
- [32] Ostapchenko, S., Monte Carlo treatment of hadronic interactions in enhanced Pomeron scheme: QGSJET-II model, *Phys. Rev. D* 83 (2011) 014018. [arXiv:1010.1869](#), [doi:10.1103/PhysRevD.83.014018](#).
- [33] Gilmore, R.C., Somerville, R.S., Primack, J.R., Domínguez, A., Semi-analytic modelling of the extragalactic background light and consequences for extragalactic gamma-ray spectra, *Mon. Not. R. Astron. Soc.* 422 (4) (2012) 3189–3207. [arXiv:1104.0671](#), [doi:10.1111/j.1365-2966.2012.20841.x](#).
- [34] Protheroe, R.J. and Biermann, P.L., A new estimate of the extragalactic radio background and implications for ultra-high-energy  $\gamma$ -ray propagation, *Astropart. Phys.* 6 (1996) 45–54, [Erratum: *Astropart. Phys.* 7, 181 (1997)]. [arXiv:astro-ph/9605119](#), [doi:10.1016/S0927-6505\(96\)00041-2](#).
- [35] Settimo, M. and De Domenico, M., Propagation of extragalactic photons at ultra-high energy with the *EleCa* code, *Astropart. Phys.* 62 (2015) 92–99. [arXiv:1311.6140](#), [doi:10.1016/j.astropartphys.2014.07.011](#).
- [36] Lee, S., On the propagation of extragalactic high energy cosmic and  $\gamma$  rays, *Phys. Rev. D* 58 (1998) 043004. [arXiv:astro-ph/9604098](#), [doi:10.1103/PhysRevD.58.043004](#).
- [37] Aab, A., et al., Combined fit of spectrum and composition data as measured by the Pierre Auger Observatory, *J. Cosmol. Astropart. Phys.* 04 (2017) 038, [Erratum: *JCAP* 03, E02 (2018)]. [arXiv:1612.07155](#), [doi:10.1088/1475-7516/2017/04/038](#).
- [38] Abdul Halim, A., et al., Constraining the sources of ultra-high-energy cosmic rays across and above the ankle with the spectrum and composition data measured at the Pierre Auger Observatory, *J. Cosmol. Astropart. Phys.* 05 (2023) 024. [arXiv:2211.02857](#), [doi:10.1088/1475-7516/2023/05/024](#).
- [39] Abdul Halim, A., et al., Impact of the Magnetic Horizon on the Interpretation of the Pierre Auger Observatory Spectrum and Composition Data, *arXiv e-prints* [arXiv:2404.03533](#), [doi:10.48550/arXiv.2404.03533](#).
- [40] Adam, R., et al., *Planck* 2015 results - I. Overview of products and scientific results, *Astron. Astrophys.* 594 (2016) A1. [arXiv:1502.01582](#), [doi:10.1051/0004-6361/201527101](#).
- [41] Aab, A., et al., Evidence for a mixed mass composition at the ‘ankle’ in the cosmic-ray spectrum, *Phys. Lett. B* 762 (2016) 288–295. [arXiv:1609.08567](#), [doi:10.1016/j.physletb.2016.09.039](#).
- [42] Abbasi, R.U., et al., Study of muons from ultrahigh energy cosmic ray air showers measured with the Telescope Array experiment, *Phys. Rev. D* 98 (2) (2018) 022002. [arXiv:1804.03877](#), [doi:10.1103/PhysRevD.98.022002](#).
- [43] Abdul Halim, A., et al., Testing hadronic-model predictions of depth of maximum of air-shower profiles and ground-particle signals using hybrid data of the Pierre Auger Observatory, *Phys. Rev. D* 109 (2024) 102001. [arXiv:2401.10740](#), [doi:10.1103/PhysRevD.109.102001](#).
- [44] Virtanen, P., et al., SciPy 1.0: fundamental algorithms for scientific computing in Python, *Nat. Methods* 17 (2020) 261–272. [arXiv:1907.10121](#), [doi:10.1038/s41592-019-0686-2](#).
- [45] Storn, R., Price, K., Differential Evolution – A Simple and Efficient Heuristic for Global Optimization over Continuous Spaces, *J. Glob. Optim.* 11 (4) (1997) 341–359. [doi:10.1023/A:1008202821328](#).
- [46] Alves Batista, R., et al., Effects of uncertainties in simulations of extragalactic UHECR propagation, using CRPropa and SimProp, *J. Cosmol. Astropart. Phys.* 10 (2015) 063. [arXiv:1508.01824](#), [doi:10.1088/1475-7516/2015/10/063](#).
- [47] Abreu, P., et al., A Search for Photons with Energies Above  $2 \times 10^{17}$  eV Using Hybrid Data from the Low-Energy Extensions of the Pierre Auger Observatory, *Astrophys. J.* 933 (2) (2022) 125. [arXiv:2205.14864](#), [doi:10.3847/1538-4357/ac7393](#).
- [48] Aartsen, M.G., et al., Differential limit on the extremely-high-energy cosmic neutrino flux in the presence of astrophysical background from nine years of IceCube data, *Phys. Rev. D* 98 (6) (2018) 062003. [arXiv:1807.01820](#), [doi:10.1103/PhysRevD.98.062003](#).
- [49] Aab, A., et al., Probing the origin of ultra-high-energy cosmic rays with neutrinos in the EeV energy range using the Pierre Auger Observatory, *J. Cosmol. Astropart. Phys.* 10 (2019) 022. [arXiv:1906.07422](#), [doi:10.1088/1475-7516/2019/10/022](#).
- [50] Kotera, K., Allard, D., Olinto, A.V., Cosmogenic neutrinos: parameter space and detectability from PeV to ZeV, *J. Cosmol. Astropart. Phys.* 2010 (10) (2010) 013. [arXiv:1009.1382](#), [doi:10.1088/1475-7516/2010/10/013](#).
- [51] Abbasi, R.U., et al., Evidence for a Supergalactic Structure of Magnetic Deflection Multiplets of Ultra-high-energy Cosmic Rays, *Astrophys. J.* 899 (1) (2020) 86. [arXiv:2005.07312](#), [doi:10.3847/1538-4357/aba26c](#).

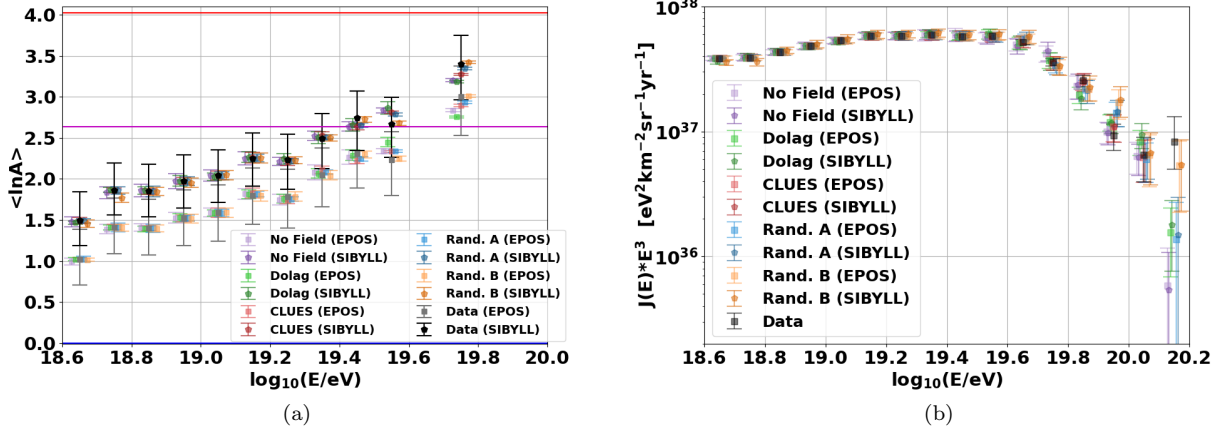


Figure 10: The evolving fraction combined fit results for all simulated magnetic fields and two EAS models (EPOS-LHC (EPOS) and Sibyll-2.3c (SIBYLL)) compared to Auger data [27, 28]. Slight offsets are applied in the x-axis for improved visibility. (a) Mean log mass number  $\langle \ln A \rangle$ . Horizontal lines are blue:proton, magenta:nitrogen, and red:iron. (b) Energy spectra multiplied by  $E^3$  for visibility.

Evolving Fraction Energy Spectrum Parameters

Field	Model	$\Sigma\chi^2/\text{bin}$	$\gamma$	$\log_{10}(R_{\text{cut}}/V)$	$D_{\text{cut}}/\text{Mpc}$	$n$
No Field	SIBYLL	0.370	$2.10^{+0.47}_{-0.14}$	$19.19^{+0.84}_{-0.20}$	$844^{+0}_{-1}$	$1.344^{+0.014}_{-0.005}$
	EPOS	0.326	$1.94^{+0.60}_{-0}$	$19.22^{+0.75}_{-0.01}$	$844^{+0}_{-1}$	$1.343^{+0.006}_{-0.005}$
Dolag	SIBYLL	0.469	$2.28^{+0.14}_{-0.84}$	$19.89^{+0.31}_{-0.98}$	$907^{+450}_{-50}$	$1.328^{+0.023}_{-0.000}$
	EPOS	0.446	$2.31^{+0.12}_{-0.20}$	$19.89^{+0.40}_{-0.38}$	$889^{+146}_{-39}$	$1.342^{+0.006}_{-0.011}$
CLUES	SIBYLL	0.307	$2.65^{+0.00}_{-0.29}$	$19.58^{+0.27}_{-0.25}$	$841^{+1}_{-0}$	$1.342^{+0.013}_{-0.007}$
	EPOS	0.295	$2.52^{+0.09}_{-0.22}$	$19.58^{+0.51}_{-0.20}$	$842^{+0}_{-1}$	$1.342^{+0.006}_{-0.004}$
Rand.A	SIBYLL	0.344	$2.64^{+0.20}_{-0.25}$	$19.95^{+0.50}_{-0.56}$	$855^{+93}_{-7}$	$1.343^{+0.008}_{-0.005}$
	EPOS	0.341	$2.65^{+0.05}_{-0.30}$	$19.89^{+0.94}_{-0.32}$	$844^{+113}_{-0}$	$1.342^{+0.006}_{-0.006}$
Rand.B	SIBYLL	0.236	$2.35^{+0.34}_{-0.30}$	$19.40^{+1.64}_{-0.32}$	$843^{+171}_{-0}$	$1.346^{+0.009}_{-0.006}$
	EPOS	0.237	$2.21^{+0.34}_{-0.45}$	$19.51^{+1.20}_{-0.38}$	$843^{+174}_{-0}$	$1.342^{+0.004}_{-0.007}$

Table 5: The FR0 evolving fraction combined fit results total sum chi-square per bin, spectral index  $\gamma$ , exponential rigidity cutoff ( $\log_{10}(R_{\text{cut}})$ ), trajectory cutoff ( $D_{\text{cut}}$ ), and spectrum normalization for all 10 configurations. The two EAS are EPOS-LHC (EPOS) and Sibyll2.3c (SIBYLL).

Evolving Fraction Bootstrap Energy Spectrum Parameters

Field	Model	$\Sigma\chi^2/\text{bin}$	$\gamma$	$\log_{10}(R_{\text{cut}}/V)$	$D_{\text{cut}}/\text{Mpc}$	$n$
No Field	SIBYLL	0.370	$2.44^{+0.23}_{-0.23}$	$19.34^{+0.25}_{-0.25}$	$843^{+0}_{-0}$	$1.345^{+0.006}_{-0.006}$
	EPOS	0.326	$2.47^{+0.12}_{-0.12}$	$19.40^{+0.10}_{-0.10}$	$843^{+0}_{-0}$	$1.340^{+0.004}_{-0.004}$
Dolag	SIBYLL	0.469	$2.26^{+0.28}_{-0.28}$	$19.23^{+0.25}_{-0.25}$	$867^{+193}_{-193}$	$1.335^{+0.004}_{-0.004}$
	EPOS	0.446	$2.26^{+0.19}_{-0.19}$	$19.74^{+0.18}_{-0.18}$	$890^{+107}_{-107}$	$1.341^{+0.003}_{-0.003}$
CLUES	SIBYLL	0.307	$2.40^{+0.07}_{-0.07}$	$19.71^{+0.12}_{-0.12}$	$842^{+0}_{-0}$	$1.347^{+0.013}_{-0.007}$
	EPOS	0.295	$2.34^{+0.06}_{-0.06}$	$19.68^{+0.10}_{-0.10}$	$842^{+0}_{-0}$	$1.341^{+0.005}_{-0.005}$
Rand.A	SIBYLL	0.344	$2.37^{+0.05}_{-0.05}$	$19.83^{+0.11}_{-0.11}$	$853^{+35}_{-35}$	$1.342^{+0.003}_{-0.003}$
	EPOS	0.341	$2.33^{+0.05}_{-0.05}$	$19.68^{+0.08}_{-0.08}$	$851^{+30}_{-30}$	$1.342^{+0.003}_{-0.003}$
Rand.B	SIBYLL	0.236	$2.41^{+0.10}_{-0.10}$	$19.74^{+0.41}_{-0.41}$	$850^{+43}_{-43}$	$1.348^{+0.004}_{-0.004}$
	EPOS	0.237	$2.31^{+0.11}_{-0.11}$	$19.59^{+0.20}_{-0.20}$	$853^{+49}_{-49}$	$1.345^{+0.004}_{-0.004}$

Table 6: The FR0 evolving fraction combined fit bootstrap distribution most probable spectral index  $\gamma$ , exponential rigidity cutoff ( $\log_{10}(R_{\text{cut}})$ ), trajectory cutoff ( $D_{\text{cut}}$ ), and spectrum normalization for all 10 configurations.



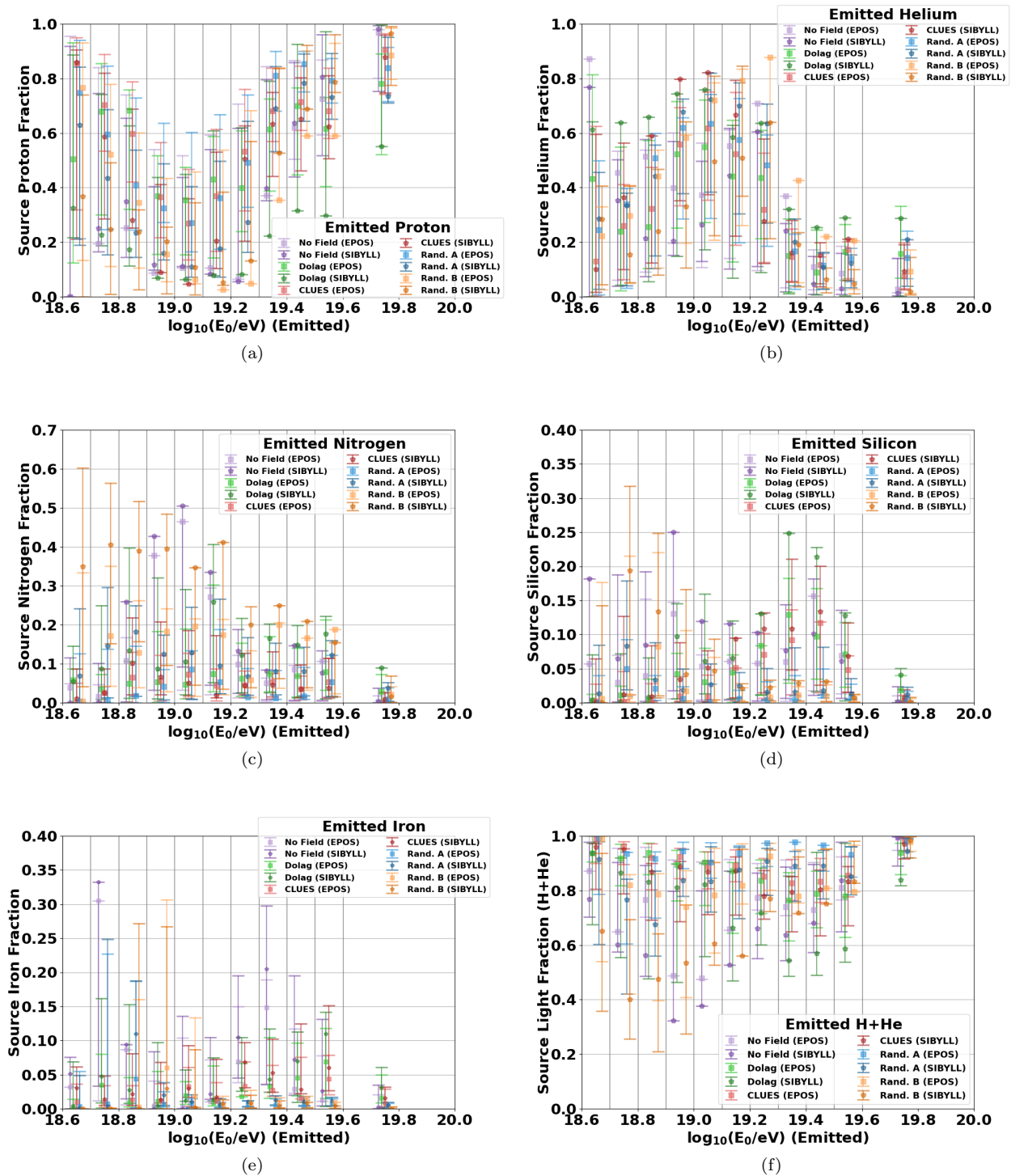


Figure 11: The evolving fraction fit FR0 emitted nuclei fractions necessary to best fit the data for ten configurations based on the EPOS-LHC (EPOS) and Sibyll2.3c (SIBYLL) hadronic interaction models versus emitted energy. Additionally, the lightest components – hydrogen plus helium are shown in (f).

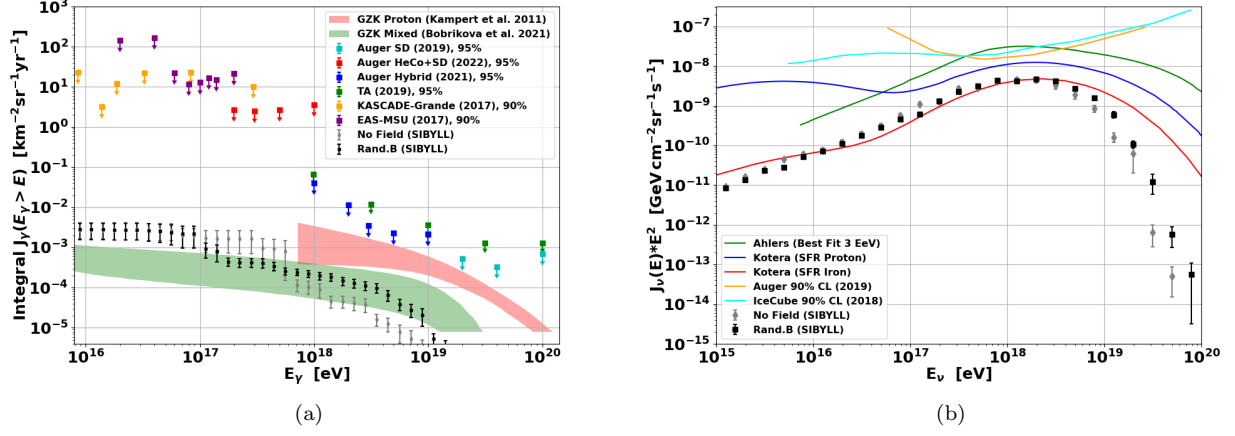


Figure 12: Evolving fraction fit cosmogenic photon and neutrino spectra for the best fit Rand.B-SIBYLL configuration (in black) compared to the no-field case (in grey). (a) Integral cosmogenic photon spectrum compared with two theoretical models and experimental upper limits as in [47]. (b) All-flavor neutrino spectrum compared with three theoretical models and experimental upper limits [48, 49, 50].

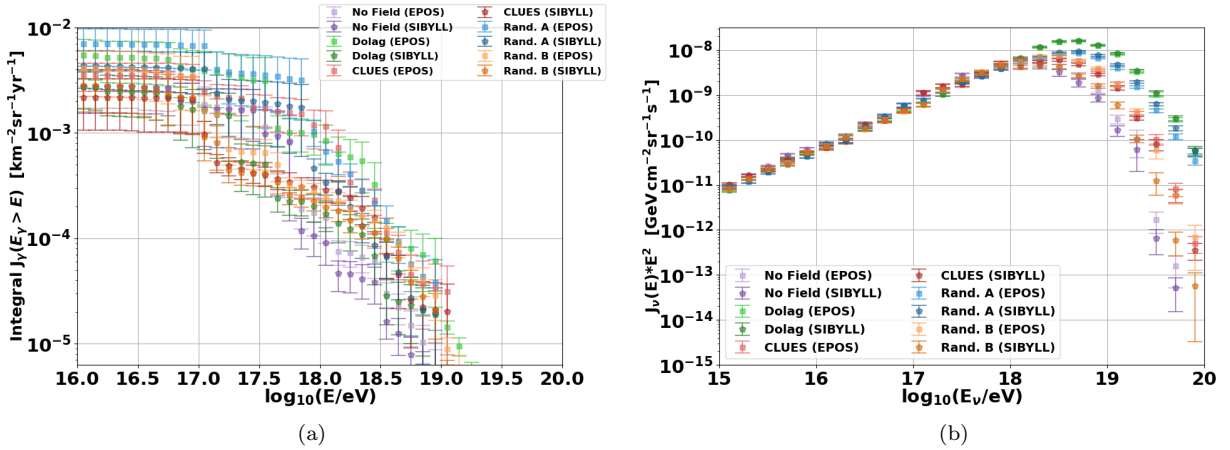
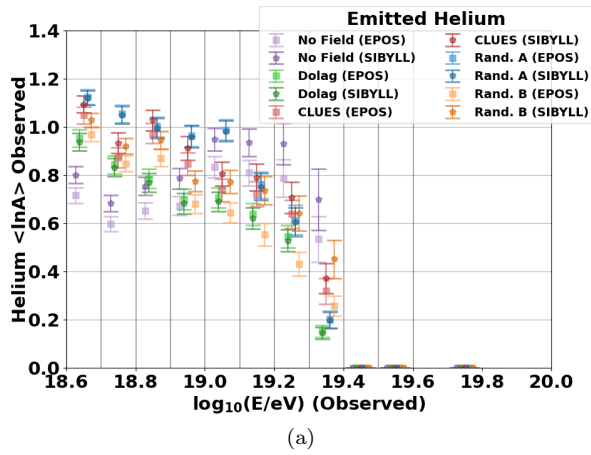


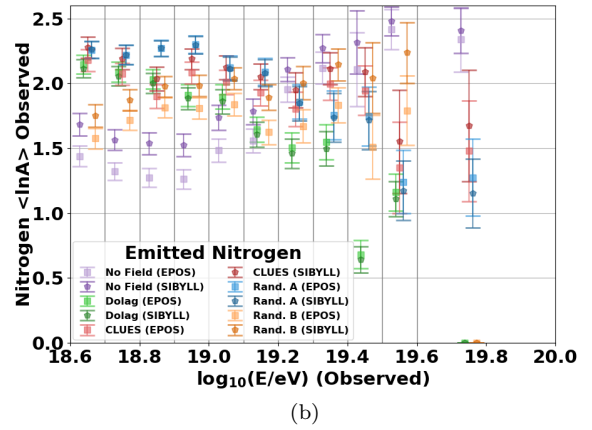
Figure 13: Evolving fraction fit cosmogenic photon and neutrino spectra for the ten configurations based on EPOS-LHC (EPOS) and Sibyll2.3c (SIBYLL) hadronic interaction models. (a) Integral cosmogenic photon spectra. (b) All-flavor neutrino spectra multiplied by  $E^2$ .

## Appendix A.

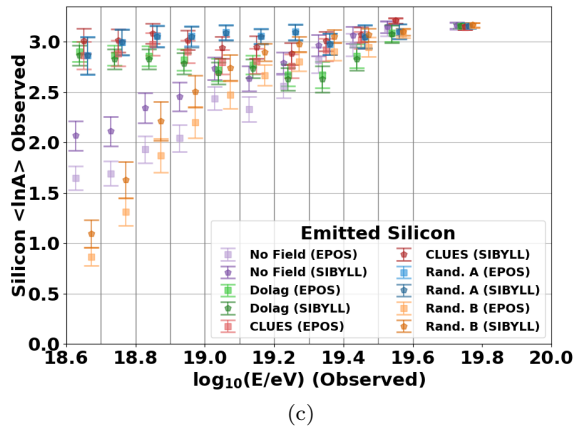
In this appendix are figures for intermediate results of the evolving fraction fits. Figure A.14 shows the resulting  $\langle \ln A \rangle$  after propagation for each emitted nuclei species for all ten configurations of magnetic field and EAS model. These are the values used to fit the composition data and have some dependence on the energy spectrum parameters. Figure A.15 shows the 44 free composition observed fraction parameters that were fit to the data. The final emission fractions (Figure 11) are the average of the observed fractions in emitted energy bins with the ratio of observed particles to those emitted taken into account (Shown in Figure A.16).



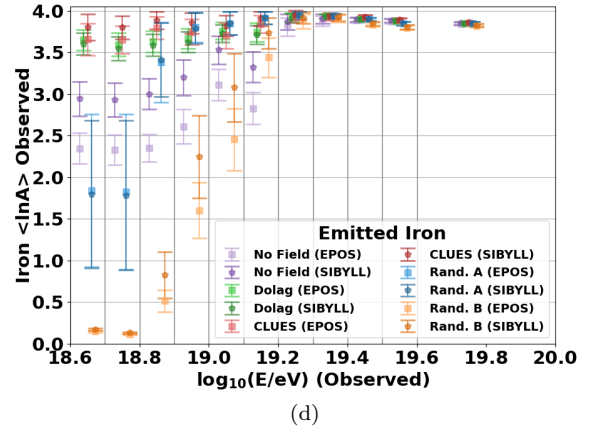
(a)



(b)

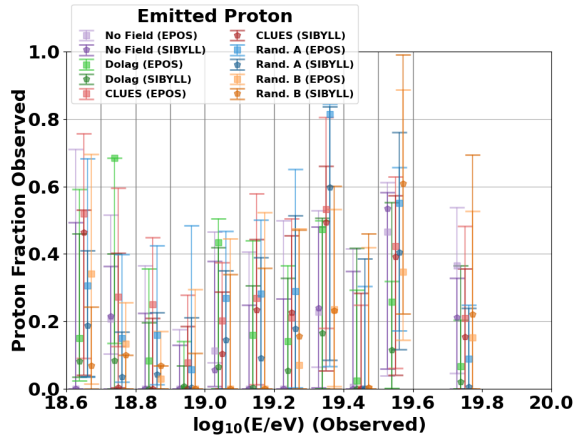


(c)

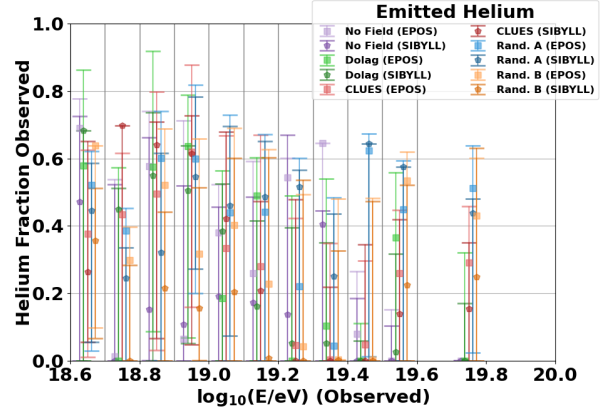


(d)

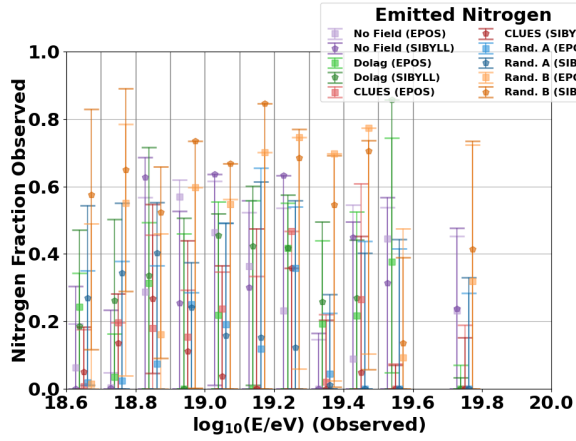
Figure A.14: The evolving fraction fit results observed  $\langle \ln A \rangle$  for all ten configurations versus emitted energy for each emitted nuclei species. Proton has a constant  $\langle \ln A \rangle = 0$ . The figures upper bounds are approximately the  $\langle \ln A \rangle$  of the emitted nuclei.



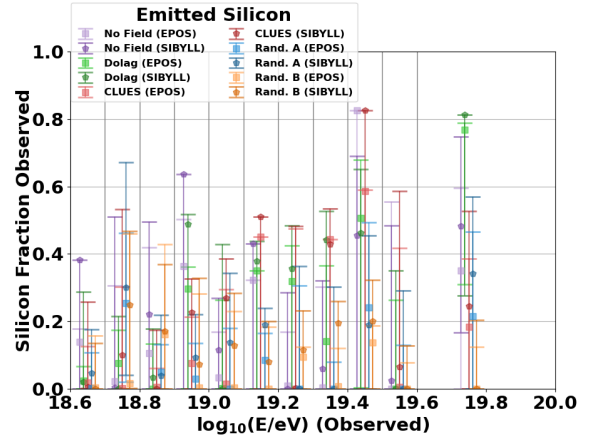
(a)



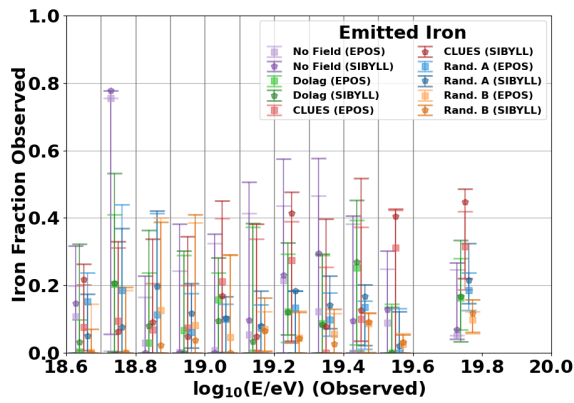
(b)



(c)

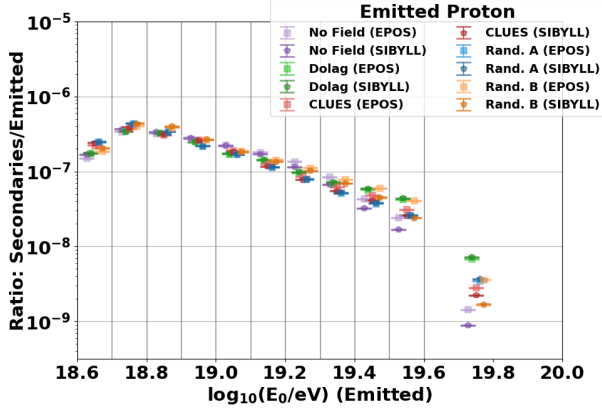


(d)

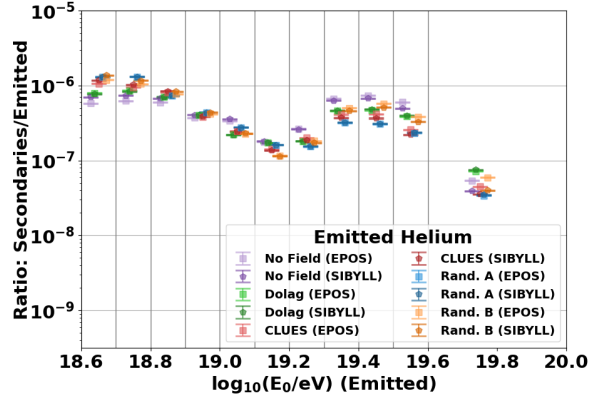


(e)

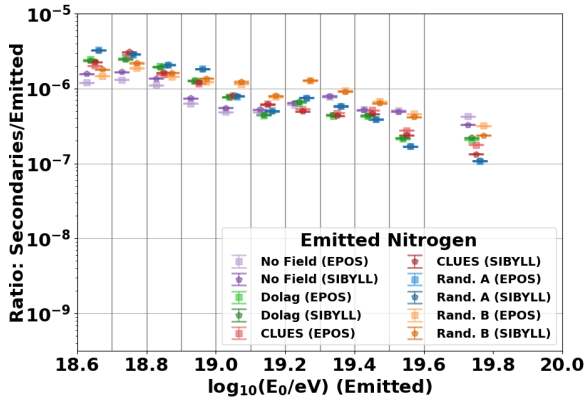
Figure A.15: The evolving fraction fit observed nuclei fraction results for all ten configurations versus observed energy. These observed fractions are the free composition parameters in the fit.



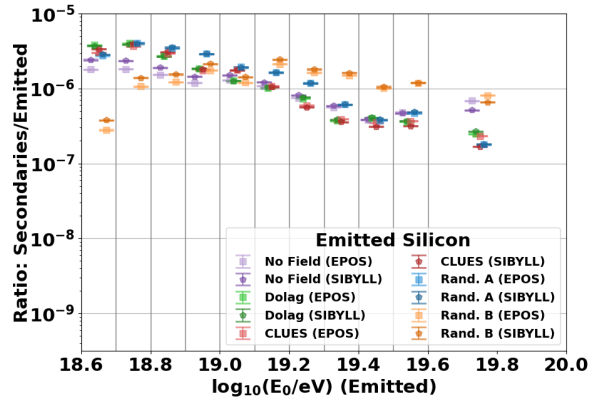
(a)



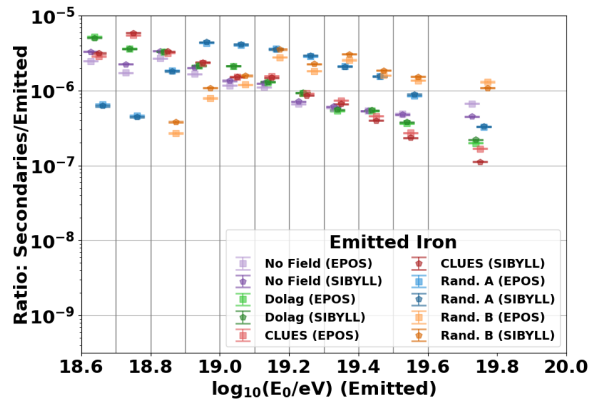
(b)



(c)



(d)



(e)

Figure A.16: The evolving fraction fit ratio of secondaries to emitted nuclei for all ten configurations versus emitted energy. The average observed nuclei fractions (Figure A.15) in emitted energy bins are converted to the emission fractions using these ratios (Shown in Figure 11).